Marc, O., Hovius, N., Meunier, P., Gorum, T., Uchida, T. (2016): A seismologically consistent expression for the total area and volume of earthquake-triggered landsliding. - *Journal of Geophysical Research*, *121*, 4, pp. 640–663.

DOI: http://doi.org/10.1002/2015JF003732

AGU PUBLICATIONS

JGR

Journal of Geophysical Research: Earth Surface

RESEARCH ARTICLE

10.1002/2015JF003732

A seismologically consistent expression for the total area and volume of earthquake-triggered landsliding

Odin Marc[1,2], Niels Hovius[1,2], Patrick Meunier[3], Tolga Gorum[4,5], and Taro Uchida[6]

[1]Helmholtz Centre Potsdam, German Research Center for Geosciences (GFZ), Telegrafenberg, Potsdam, Germany, [2]Institute of Earth and Environmental Science, University of Potsdam, Potsdam, Germany, [3]Ecole Normale Suprieure de Paris, Laboratoire de Gologie, Paris CEDEX 5, France, [4]Faculty of Geo-Information Science and Earth Observation (ITC), University of Twente, AE, Enschede, Netherlands, [5]Now at Istanbul University, Department of Geography, Istanbul, Turkey, [6]National Institute for Land and Infrastructure Management, Research Center for Disaster Risk Management, 1 Asahi, Tsukuba, Japan

Key Points:
- Earthquake-triggered landsliding modeled based on seismological laws
- Predictions tested against data from 40 earthquakes
- Landscape steepness control over triggered slope failure empirically quantified

Supporting Information:
- Supporting Information S1
- Table S1

Correspondence to:
O. Marc,
omarc@gfz-potsdam.de

Citation:
Marc, O., N. Hovius, P. Meunier, T. Gorum, and T. Uchida (2016), A seismologically consistent expression for the total area and volume of earthquake-triggered landsliding, *J. Geophys. Res. Earth Surf.*, *121*, 640–663, doi:10.1002/2015JF003732.

Received 17 SEP 2015
Accepted 30 MAR 2016
Accepted article online 6 APR 2016
Published online 21 APR 2016

Abstract We present a new, seismologically consistent expression for the total area and volume of populations of earthquake-triggered landslides. This model builds on a set of scaling relationships between key parameters, such as landslide spatial density, seismic ground acceleration, fault length, earthquake source depth, and seismic moment. To assess the model we have assembled and normalized a catalog of landslide inventories for 40 shallow, continental earthquakes. Low landscape steepness causes systematic overprediction of the total area and volume of landslides. When this effect is accounted for, the model predicts the total landslide volume of 63% of 40 cases to within a factor 2 of the volume estimated from observations ($R^2 = 0.76$). The prediction of total landslide area is also sensitive to the landscape steepness, but less so than the total volume, and it appears to be sensitive to controls on the landslide size-frequency distribution, and possibly the shaking duration. Some outliers are likely associated with exceptionally strong rock mass in the epicentral area, while others may be related to seismic source complexities ignored by the model. However, the close match between prediction and estimate for about two thirds of cases in our database suggests that rock mass strength is similar in many cases and that our simple seismic model is often adequate, despite the variety of lithologies and tectonic settings covered. This makes our expression suitable for integration into landscape evolution models and application to the anticipation or rapid assessment of secondary hazards associated with earthquakes.

1. Introduction

Seismically triggered landslides are a major hazard and cause of secondary losses associated with earthquakes, with effects sometimes exceeding those of direct shaking [*Bird and Bommer*, 2004]. Moreover, due to widespread triggered landsliding, earthquakes can be important drivers of continental erosion [*Keefer*, 1994; *Malamud et al.*, 2004] and they have been found to be important actors in mountain building and landscape evolution [*Hovius et al.*, 2011; *Li et al.*, 2014]. Models permitting the prediction or rapid estimation of the total area or total volume of landsliding due to earthquakes can therefore aid in seismic hazard assessment and disaster management as well as explorations of landscape evolution in tectonically active settings. Not surprisingly, seismic moment has been shown to be a first-order control on the area affected by landsliding [*Keefer*, 1984; *Rodriguez et al.*, 1999] and the total volume of triggered landslides [*Keefer*, 1994]. However, the scatter in simple relations between total landslide volume and earthquake moment amounts to an order of magnitude at least. This is because the spatial density of coseismic landslides is, all else being equal, set by the intensity of ground shaking [*Meunier et al.*, 2007]. Therefore, seismic wave attenuation and site effects determine the spatial distribution of landslides in detail [*Meunier et al.*, 2008, 2013]. Hence, a predictive and accurate model for the total volume of landslides caused by earthquakes should incorporate not only the earthquake magnitude [e.g., *Keefer*, 1994] but also effects such as the loss of seismic wave energy with distance from source or the nonlinear scaling between seismic moment and ground shaking. Importantly, the effects of strong motion are modulated by the local topographic slope and the effective strength of its substrate [e.g., *Parise and Jibson*, 2000; *Yagi et al.*, 2009; *Gorum et al.*, 2011, 2013]. These parameters are at the core of slope stability analysis [e.g., *Newmark*, 1965], which, although simplified, offers a physical description

of the probability of failure of a given slope during an earthquake. Ultimately, then, knowledge of the earthquake rupture initiation and propagation, translated into a model of ground shaking accurate at the hillslope scale and coupled with a robust slope stability analysis, would allow prediction of landslide areas and volumes without empirical calibration. Efforts to predict slope failure have mainly taken the form of pseudostatic [e.g., *Terzaghi*, 1950], stress-deformation [e.g., *Clough and Chopra*, 1966], and permanent displacement [e.g., *Newmark*, 1965] analyses, the rationale, advantages, and limitations of which have been comprehensively reviewed by *Jibson* [2011]. These approaches require extensive and detailed knowledge of the spatial distribution of ground shaking, topographically induced driving stresses, and of the local rock mass strength [*Dreyfus et al.*, 2013]. It is, therefore, impractical at larger scales, even if recent work suggests that it can be used to invert rock strength a posteriori [*Gallen et al.*, 2015]. In the absence of the required local knowledge, a priori, we propose not to model individual slope failures and introduce a model based on average properties of the forcing mechanism (i.e., the shaking) and of the landscape (i.e., steepness, strength, and hydrology) on which it acts. Our model aims at the prediction of the bulk response of a landscape to earthquake strong ground motion, giving the total volume and area of the population of triggered landslides, based on seismological scaling relationships and empirically adjusted for geomorphic sensitivity. It should allow for estimation of secondary risks associated with an earthquake scenario with reduced predictive uncertainties and for improved evaluation of the role of climatic and seismic forcing of erosion in mountain belts where landsliding is the dominant erosion mechanism [*Hovius et al.*, 1997]. To determine the accuracy of this model, we have calibrated it against a compilation of landslide inventories for 40 earthquakes for which the required seismological information was available.

In this paper, we summarize the available landslide inventories and the methods used to obtain conservative estimates of total landslide volume they represent. Then, we derive a seismologically consistent model predicting total landslide area and volume for a given earthquake and landscape. To support this, we constrain empirically the link between the probability distribution of the topographic slopes in an earthquake area and the landscape response to seismic shaking. Finally, precision and limitations of the model are discussed before we close with two example applications, exploring the possible landsliding triggered by an expected earthquake scenario for the Alpine Fault, bounding the Southern Alps of New Zealand and by the 2015 M_w7.8 Gorkha earthquake in Nepal.

2. Data and Methods

2.1. Earthquake and Landslide Data

We compiled previously published information allowing estimation of total landslide area, *A*, and/or volume, *V*, for 40 shallow (<25 km), onshore earthquakes (section 2.2 and Figure S1 and Table S1 in the supporting information). The estimated numbers of triggered landslides range from $\sim10^2$ to $\sim10^5$ per event, affecting a wide range of climates (from arid to tropical to periglacial), lithologies (from carbonates to volcanic rocks and metasediments), and topographies (from active mountain ranges to fjords and volcanic landscapes). All types of landslides were considered, and most inventories contain soil, mixed, and bedrock landslides and do not explicitly discriminate between them. Mapped landslides had variable amounts of displacement, but fissures and other disturbance with negligible displacement (<1 m) are ignored. Consideration of the complexities associated with individual landslide mechanisms and landslide travel distance are beyond the scope of this paper. For 10 cases, *V* could be derived from published landslide area inventories [*Harp et al.*, 1981; *Harp and Jibson*, 1996; *Liao and Lee*, 2000; *Yagi et al.*, 2007, 2009; *Meunier et al.*, 2008; *PWRI*, 2009; *Gorum et al.*, 2011, 2013, 2014], using empirical V-A relationships [*Larsen et al.*, 2010]. To this, we added the case of the 1991 Limon (Costa Rica) earthquake, for which we mapped the landslides from 30 m resolution Landsat images (Figure S2). These 11 inventories consist of mapped polygons delineating areas disturbed by landslides (i.e., scar, runout, and deposit) but excluding debris flow transport and deposition along channels. They were scanned and corrected for mapping errors including amalgamation [*Marc and Hovius*, 2015] and for completeness for landslides larger than 10,000 m^2, which dominate the total eroded volume [*Hovius et al.*, 1997]. The 29 other cases are less well constrained, because *V* was extrapolated based on published area-frequency distributions or on information about a limited number of large landslides [*Bonilla*, 1960; *Govi and Sorzana*, 1977; *Pearce and O'Loughlin*, 1985; *Harp and Jibson*, 1996; *Jibson et al.*, 1994; *Keefer*, 1994; *Schuster et al.*, 1996; *Hancox et al.*, 1997; *Antonini et al.*, 2002; *Hancox et al.*, 2003, 2004; *Jibson and Harp*, 2006; *Mahdavifar et al.*, 2006; *Owen et al.*, 2008; *Evans et al.*, 2009; *Guzzetti et al.*, 2009; *Alfaro et al.*, 2012; *Has et al.*, 2012; *Gorum et al.*, 2014; *Xu et al.*, 2014a, 2014b; *Barlow et al.*, 2015; *Tang et al.*, 2015] (see Tables S1 and S2). Using landslide density

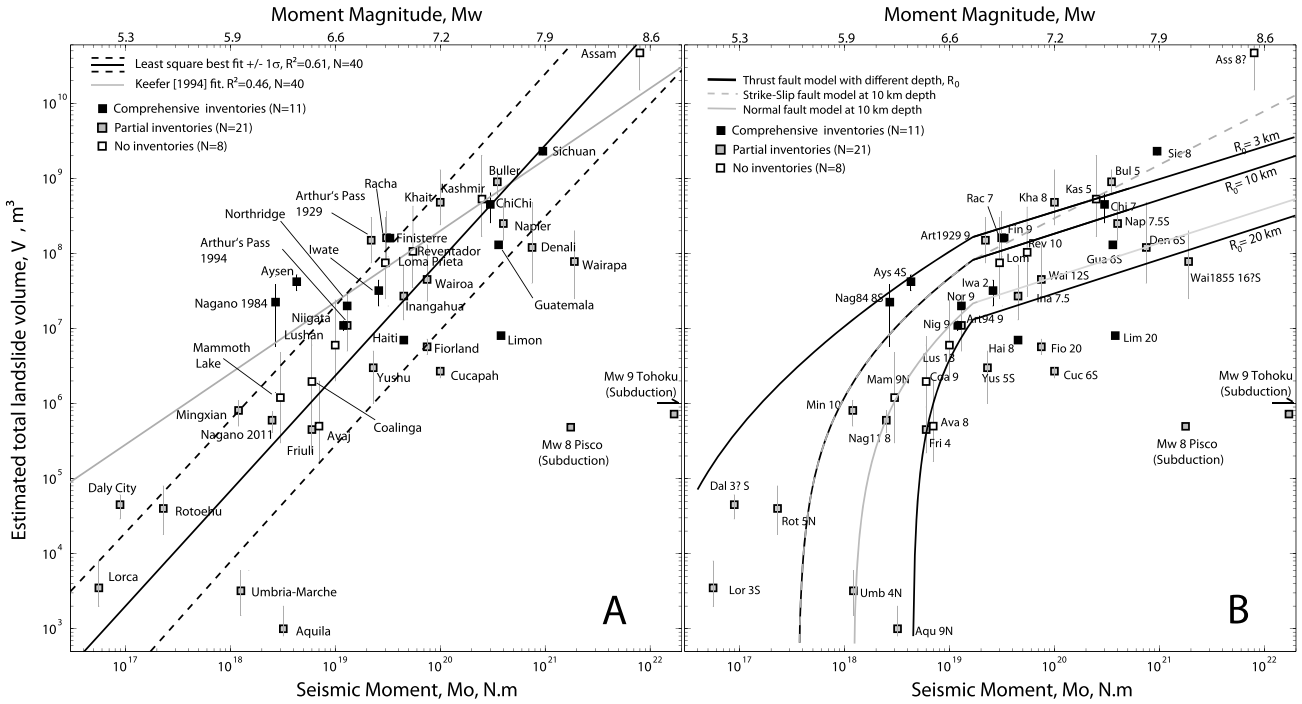

Figure 1. (a) Estimated total landslide volume with $2-\sigma$ uncertainties plotted against seismic moment for 40 shallow continental earthquakes (Table S1). The gray line is the empirical relationship proposed by *Keefer* [1994], derived from a smaller database. The solid and dotted lines are the orthogonal least squares best fit to our data set and its $1-\sigma$ uncertainties. (b) Comparison of the same data with our seismologically consistent model. The model lines do not depend on any fitted parameters but only on earthquake observables. Name codes abbreviated to their first three characters, followed by the mean asperity depth and *S* or *N* for strike slip or normal events, respectively. The three black lines represent our analytical prediction of landslide volume dependency in moment for various mean asperity depths, R_0. The solid and dashed gray lines represent our predictions for normal and strike-slip fault mechanisms, respectively, for asperities at 10 km depth. For reference, the estimated total volumes of two subduction earthquakes (Tohoku (Japan) and Pisco (Chile)) are plotted. Published landslide area-frequency distributions [*Lacroix et al.*, 2013; *Wartman et al.*, 2013] were converted to volume, using the relationship of *Larsen et al.* [2010] and integrated to obtain the estimated total volume. The estimated volumes are similar to those of shallower, continental M_w 6 earthquakes in our data base.

gradients away from seismogenic faults or earthquake epicenters, we have ascertained that all comprehensive inventories and detailed field reports in our catalog have sufficient spatial coverage to capture the bulk of landsliding caused by an earthquake [cf. *Meunier et al.*, 2007]. Amongst the 40 cases in our database, the total landslide area, *A*, could be constrained only for the 11 comprehensive inventories and six further cases with detailed mapping of large and intermediate size landslides (Table S1). In the other 23 cases, information was limited to the larger landslides, which tend to dominate the total landslide volume, but not the total area. As an example, in our 11 comprehensive inventories, the 1% largest landslides represent $53\pm22\%$ of *V* but only $21\pm8\%$ of *A*.

Though other studies have considered relations between the total landslide number and earthquakes parameters [*Keefer*, 2002; *Gorum et al.*, 2014], we did not focus on this statistic because we consider it the most ill-constrained. Importantly, the total landslide number is dominated by the smallest landslides. Such landslides are not systematically accessible for most earthquakes and tend to be easily censored or amalgamated even with recent imagery [*Stark and Hovius*, 2001; *Marc and Hovius*, 2015]. Therefore, even if the total landslide number is an important variable for landslide hazard, the available counts are not sufficiently robust in most cases, and we do not attempt to analyze or model them.

Our database includes earthquakes ranging from moment magnitude M_w 5 to 8.6 (Figure 1). These are mostly reverse fault earthquakes ($N = 25$) but also strike slip ($N = 11$) and normal fault events ($N = 4$), as determined from their focal mechanism. The hypocentral depths range from a few km to 24 km. However, it has been shown that the pattern of landsliding in two particularly well-constrained earthquakes is best explained by considering the main slip patch rather than the hypocenter as the dominant wave source [*Meunier et al.*, 2013]. From a seismological point of view, asperities on which most of the coseismic slip occurs are considered to be an important source of high-frequency waves (>0.5 Hz) [*Ruiz et al.*, 2011; *Avouac et al.*, 2015], that we

consider dominant for landslide triggering (see section 3.2). For about half of the earthquakes in our database, the mean asperity depth along the fault rupture, R_0, could be estimated from published seismological rupture inversions [*Yoshida and Koketsu*, 1990; *Wald et al.*, 1991, 1996; *Zeng and Chen*, 2001; *Hernandez et al.*, 2004; *Hikima and Koketsu*, 2005; *Pathier et al.*, 2006; *Tan and Taymaz*, 2006; *Elliott et al.*, 2007; *Cirella et al.*, 2009; *Hashimoto et al.*, 2011; *Wei et al.*, 2011; *Cheloni et al.*, 2012; *Fielding et al.*, 2013; *Sun et al.*, 2013; *Zhang et al.*, 2014] (Table S1). For less constrained cases, we set R_0 at the hypocenter [*Given et al.*, 1982; *Kawakatsu and Cadena*, 1991; *Kikuchi and Kanamori*, 1991; *Stein and Ekström*, 1992; *Anderson et al.*, 1994; *Stevens et al.*, 1998; *Doser et al.*, 1999; *Abercrombie et al.*, 2000; *McGinty et al.*, 2001; *Januzakov et al.*, 2003; *Berryman and Villamor*, 2004; *Hancox et al.*, 2004; *Hamzehloo*, 2005; *Legrand et al.*, 2011; *Alfaro et al.*, 2012; *Has et al.*, 2012] or at half the hypocentral depth when surface rupture occurred or when the earthquake exceeded M_w 7.5, accounting for the fact that for large earthquakes, rupture often propagates toward the surface, with large amount of slip occurring significantly shallower than the hypocenter. This holds for the large earthquakes for which we have the complete slip distribution but is not universal, the 1991 Limon (Costa Rica) case being an exception. The Limon earthquake ruptured a listric fault with a hypocenter at ~24 km depth, on a flat detachment, which steepened sharply offshore [*Suarez et al.*, 1995]. Seismological evidence indicates that in this earthquake, most of the moment was released at 15–20 km North of the hypocenter, along the flat detachment, and therefore, we have set the mean asperity depth at 20 km [*Goes et al.*, 1993]. Under constrained events were assigned a larger uncertainty in the modeling (Table S1). Three events are very poorly constrained and we did not set a single mean asperity depth but rather a range of 1.5 to 4.5 km, 4 to 12 km, and 8 to 24 km for the 1957 Daly City (USA), the 1950 Assam (India), and the 1855 Wairapa (New Zealand, NZ) earthquakes, respectively [*Bonilla*, 1960; *Molnar and Qidong*, 1984; *Darby and Beanland*, 1992].

We assume that this database is sufficiently large and comprehensive to distinguish first-order controls on earthquake-triggered landsliding from local, secondary effects.

2.2. Estimation of Total Landslide Volume

We used published area-volume relationships, $V' = \lambda A'^{\gamma}$ [*Larsen et al.*, 2010], to estimate the volume of a landslide, V', from its mapped disturbed area, A'. Following *Larsen et al.* [2010], it was assumed that landslides with $A' > 10^5$ m^2 involved bedrock and that smaller landslides were mixed bedrock and soil failures. Landslide maps typically do not distinguish between scar and deposit, lumping the two in one area measure, although the relevant volume, in fact, would be that of the landslide scar. As a systematic way to constrain runout variations is not available, we have applied a blanket correction to reduce the total area of a landslide to its scar area, thus obtaining a conservative volume estimate. According to *Larsen et al.* [2010], scars and deposits have area-volume relations with the same power law exponent, implying constant size ratios between scar and deposit areas of 1.1 and 1.9 for mixed and bedrock landslides, respectively. Hence, we estimated the scar area by dividing the mapped landslide area by 2.1 and 2.9 for mixed soil and bedrock and solely bedrock landslides, respectively, assuming that runout distance was equal to the scar length. This may lead to an overestimation of landslide scar volume where runout was much longer, mostly for small slides, which do not contribute significantly to the total eroded mass. Conversely, some large landslides on gentle slopes have overlapping scar and deposit areas, meaning that our correction may cause significant underestimation of the scar size and thus the landslide volume.

Rare field estimates of the volume of one or a few large earthquake-triggered landslides agree with our landslide volume estimates, supporting our assumption of a reduced proportionality of perturbed area to scar area. In Nagano, the mapping was based on airphoto interpretation and seems restricted to scar areas. In this case, the uncorrected mapped area of the landslide on Ontake volcano gave a volume estimate of $\sim 2.0 \times 10^{-2}$ km^3, closer to the field estimate of $\sim 3.4 \times 10^{-2}$ km^3 [*Voight and Sousa*, 1994]. Therefore, we did not apply an area correction to estimate the scar areas in this inventory.

We calculated the volume of every individual landslide in a catalog and summed to obtain a total volume of landslides for each earthquake. Uncertainties in our approach include the coefficient and exponent of the landslide area-volume relations, with reported standard deviations of 0.005 for both σ_λ and σ_γ for mixed bedrock-soil landslides and of 0.02 and 0.03 on σ_λ and σ_γ, respectively, for bedrock landslide scars [*Larsen et al.*, 2010]. For mapping errors, a standard deviation of 20% of the mapped area was arbitrarily assumed. Assuming no covariance between these three sources of uncertainties, we used Gaussian propagation of error to obtain $1-\sigma$ uncertainties on the volume of each mapped landslide, V'. Further, the standard deviation on the total landslide volume for an earthquake was calculated assuming that the volume of each individual landslide

was unrelated to that of any other, ignoring possible covariance. Hence, the uncertainty on the total volume, reported in Table S1, depends heavily on the size distribution of landslides. When the total landslide volume is dominated by many medium-sized landslides in a population, then the uncertainty on the total volume estimate is small, because it is unlikely that all important individual landslide volumes are biased in the same way (e.g., the 1994 Northridge (USA) and 2010 Haiti (Haiti) cases). However, when the total volume is dominated by a few very large landslides, then the uncertainties on their volumes are less likely to cancel out, which leads to a large uncertainty on the total volume estimate (e.g., 1984 Nagano (Japan) and 2008 Iwate (Japan) cases).

For earthquakes without exhaustive landslide inventories we estimated the total landslide volume using one of the following methods. In the best cases, published area-frequency distributions were used to estimate the number of landslides for a given size range and converted to volumes as outlined above. However, for most larger earthquakes, volumes were reported only for a limited number of very large landslides, typically <20 landslides $>5.0 \times 10^{-4}$ km^3 (Table S2). For comparison, in eight of our 11 comprehensive inventories the 10 largest landslides comprised 20% to 86% of the total landslide volume, V, and $51 \pm 23\%$ on average, excluding the Haiti, Northridge, and Limon cases, which did not have any landslides larger than 5.0×10^{-4} km^3. Hence, in some cases all the small landslides together could have a smaller volume than the uncertainties on the volume of the large landslides, but in other cases the total volume of small landslides could be five times that of the large ones. For simplicity, we assumed that the reported landslides were indeed the largest, that their volume V_L represented ~66% of V, and that the $2-\sigma$ uncertainty range of V extends between 75% and 400% of V_L, accounting for the uncertainties on the total landslide volume estimate. Finally, for a few earthquakes (1950 Assam (India), 1989 Loma Prieta (USA), 1987 Reventador (Ecuador), 1980 Mammoth (USA), and 1983 Coalinga (USA)), an estimate of the total landslide volume was published without further information on uncertainties or on the size of individual landslides and for some others (2005 Kashmir (Pakistan), 2002 Avaj (Iran), and 2013 Lushan (China)) only the largest landslide was described. Assuming a universal area-frequency distribution, a total volume can be estimated from the largest landslide [*Malamud et al.*, 2004, equations (27) and (33)]. This assumes implicitly a volume scaling that is biased upward ($V' \sim 0.05A'^{1.5}$), but given the other sources of uncertainty on the landslide area-frequency distribution and on the volume of the largest landslide, we simply use the relationship provided by *Malamud et al.* [2004]. Note that estimates from the previous methods are not inconsistent with and mostly within a factor of 3 of this crudest type of estimate (Table S2). Nevertheless, these eight cases are certainly the least constrained in our catalog, and we therefore assign to them an arbitrary uncertainty range of a factor 4, greater than the uncertainty range of any other methods (Table S2). Finally, the 2011 Lorca (Spain) and 2004 Rotoehu (NZ) earthquakes triggered only a few tens of slides and 100–200 small rock falls, and we estimated the total volume range based on field photographs and reported volumes. This too is crude, but, because of the limited number of landslides and the small size of the larger events, we consider the total landslide volume to be relatively well constrained compared with the eight uncertain cases discussed above.

2.3. Case-Specific Corrections

Robust and uniform estimation of landslide volumes from available maps relies on the accuracy and consistency of mapping between the different data sets. An issue of particular importance in this respect is amalgamation, that is, the bundling of multiple adjacent landslides into a single larger map polygon. Compounded with a landslide area-volume relation favoring the largest landslides, this can give rise to significant overestimation of the total landslide volume. We have discussed this issue, its consequences and how to detect associated mapping errors elsewhere [*Marc and Hovius*, 2015]. Here, we briefly review how individual data sets have been corrected for its effects.

Amalgamation has affected a previous estimate of the volume of landslides triggered by the 2008 Sichuan (China) earthquake [*Parker et al.*, 2011; *Li et al.*, 2014], which, at ~15 km^3, was substantially higher than our value of 2.3 ± 0.25 km^3, even though we have used a landslide covering a larger area [*Marc and Hovius*, 2015]. However, amalgamation is also evident in the mapping used for our volume estimate [*Gorum et al.*, 2011] and we manually split the largest 152 landslides of the catalog, which dominate the total volume. Because of our limited ability to comprehensively remove amalgamation across the full range of polygon sizes, the total landslide volume for the Sichuan event must be considered to have a slight upward bias. The same argument holds for the 1976 Guatemala (Guatemala), 1999 Chi-Chi (Taiwan), and 1994 Northridge (USA) earthquakes, for which the landslide inventories have been edited for amalgamation giving minimum volume reductions of 35%, 38%, and 16%, respectively [*Marc and Hovius*, 2015]. Finally, for the Aysen Fjord inventory we split 11 polygons larger than 0.1 Mm^2, including the three largest ones, into 37 and obtained a volume reduction

of 29%. Although occasional amalgamation of relatively small landslides may also affect the other data sets, it is not considered to be a major source of errors and it was not mitigated for systematically.

3. Modeling the Volume of Seismically Induced Landslides

An empirical relation between total landslide volume, *V*, and the seismic moment, *Mo*, with the form of a sublinear power law, was first presented by *Keefer* [1994]. It was based on 15 earthquakes, spanning a large range of magnitudes and hypocentral depths, including some subduction earthquakes. In assembling our extended database of 40 events, we eliminated the subduction earthquakes and focused only on continental, crustal events with an uncertainty assessment, as described in the previous section. Subduction earthquakes are typically deep (>30 km) and offshore, meaning that only a fraction of the emitted waves reach onshore high standing topography, after significant attenuation. Onshore strong ground motion in such earthquakes is commonly only moderate, yielding relatively small landslide numbers, areas, and volumes [*Lacroix et al.*, 2013; *Wartman et al.*, 2013] (Figure 1). In such cases, landsliding tends to be strongly influenced by site characteristics and site effects, negating several assumptions of our model approach. An orthogonal best fit to our data has the landslide volume scaling with the seismic moment to the power of three halves ($Mo^{3/2}$, $R^2 = 0.6$), but it does not capture all physical processes and their associated parameters, which are relevant to landsliding. More than one order of magnitude of scatter remains for a given earthquake moment (Figure 1), indicating that additional parameters affect the total volume of landslides triggered by earthquakes.

An accurate prediction of earthquake-triggered landslide volume requires the specific acknowledgment of the role of a range of seismological, topographic, and mechanical parameters. The relation between ground shaking and landsliding has now been firmly established for a number of earthquakes [*Harp and Jibson*, 2002; *Meunier et al.*, 2007; *Yuan et al.*, 2013], highlighting the need to account for wave attenuation with distance from the earthquake source. Moreover, it is clear that hillslope-scale rock strength and local topographic gradient and relief modulate the propensity to failure of a landscape undergoing shaking [e.g., *Schmidt and Montgomery*, 1996; *Parise and Jibson*, 2000; *Yagi et al.*, 2009; *Gorum et al.*, 2013]. Below, we combine recent observational constraints on earthquake-triggered landslides with seismological scaling relationships and a statistical approach to landscape sensitivity.

3.1. Model Development

Typically, earthquake-triggered landslides are considered to occur when transient driving stresses on a potential failure plane due to variable ground shaking exceed the resisting stresses [*Newmark*, 1965]. To predict the earthquake-triggered landsliding across a landscape, this approach requires the assessment of the stresses and mechanical properties over the whole topography [*Dreyfus et al.*, 2013]. We propose an alternative approach, relating landsliding primarily to strength reduction caused by ground shaking, and argue that it is adequate for modeling of landsliding at the landscape scale. We then consider effects modulating the ground shaking such as the scaling of seismic source emission with moment, the wave attenuation with distance from the source, and the scaling of the number of point sources with the fault size. In order to develop a simple analytical solution for our model, we made three major simplifications or assumptions that are discussed in section 3.2.

We neglected scattering and inelastic effects on wave attenuation and considered only geometrical spreading (Assumption 1). We assigned to the landscape above the seismogenic fault a uniform geomorphologic sensitivity and assumed the seismic directivity of the shaking may be neglected (Assumption 2). Lastly, we assumed that landslides are triggered by relatively high-frequency *S* waves (~1 Hz) (Assumption 3).

To develop our model, we start with the widely observed relationship between landsliding and ground shaking *a* [*Harp and Jibson*, 2002; *Khazai and Sitar*, 2004], using the simple statistical approach introduced by *Meunier et al.* [2007]:

$$P_{\mathrm{LSV}} = \alpha_V (a - a_c), \tag{1}$$

where P_{LSV} is the landslide volume density and α_V is a volume sensitivity term that sets the hillslope propensity to failure for a given shaking (in m^3 km^{-2}) and a_c is the minimum acceleration required for landsliding to occur. Note that throughout this study all acceleration terms are normalized by the gravitational acceleration *g* and therefore dimensionless. Equation (1) was originally proposed for landslide area, with a landslide area density P_{LSA} and area sensitivity α_A (in m^2 km^{-2}), but it holds also for a volume density and sensitivity (Figure S3). Though the original correlation in *Meunier et al.* [2007] was obtained with measured peak ground

accelerations, we propose that equation (1) holds with a being the characteristic ground acceleration in the range of frequencies relevant for landslide triggering (see section 3.2). Note also that although we focus on acceleration in this work, ground velocity and strain have also been discussed as potential landslide triggers [*Harp et al.*, 2014].

As we are interested in the cumulative volume of landslides across the landscape, a_c should be a global, relatively constant parameter, rather than vary between individual slopes. Supporting this generalization is the observation that earthquake-triggered landslides mostly occur in very steep slopes, $>35-50^\circ$ [e.g., *Parise and Jibson*, 2000; *Lin et al.*, 2008; *Gorum et al.*, 2013]. Such slopes are typically steeper than the friction angle of the underlying material and remain stable because of cohesion. In soil covered slopes, clay or vegetation promote cohesion. In bedrock, even steeper slopes (>45°) may retain some cohesion, in spite of jointing. Moreover, several studies have postulated or found nonlinear soil behavior or bedrock strength reduction, due to a drop of cohesion or dynamic friction reduction, caused by earthquake strong motion [e.g., *Wen*, 1994; *Sleep*, 2011a, 2011b; *Marc et al.*, 2015]. Therefore, we propose that a_c is the threshold acceleration at which a sudden drop of cohesion, transient or permanent, occurs in slope materials. Even if a_c may vary with the material properties at individual locations, these variations are likely much smaller than the variations of cohesion observed in different material, making it a relatively constant parameter. This assumption is supported by the fact that equation (1) holds for different earthquakes in different landscapes with an almost constant value for a_c between 0.1 and 0.2 [*Meunier et al.*, 2007; *Hovius and Meunier*, 2012; *Yuan et al.*, 2013]. It is also consistent with nonlinear soil behavior starting at 0.15 g [e.g., *Wen*, 1994].

However, the number of slope failures does not only depend on the magnitude of the shaking-induced strength reduction, but also on the frequency of slopes steeper than the friction angle and on their cohesion ambient pore pressure. Therefore, the geomorphological complexity of the exact distribution of topographic relief, slope gradients and cohesion, as well as the hydrologic influence of pore pressure in a landscape are bundled into α, while the term $a-a_c$ contains only the seismological effects controlling the ground shaking. This makes equation (1) a statistical description of a simplified slope stability analysis where the shaking term and the slope properties are separated. Explicit modeling of α is a major challenge because the landslide area and volume density depends not only on the number of slope failures but also on the mechanical processes that will define the depth and extent of the ensuing landslides [e.g., *Stark and Guzzetti*, 2009]. Below we use seismological scaling relationships to relate a to earthquake characteristics and propose a first-order empirical constraint on α based on landscape properties.

The ground shaking a mainly depends on the inferred source acceleration b (the acceleration carried by waves at 1 km from the source) and the wave attenuation between source and surface and on the site and directivity effects [*Boore and Atkinson*, 2008]. In order to derive an analytical prediction we neglect nonlinear attenuation of seismic waves (Assumption 1), considering only their geometrical spreading. We also neglect any effects of directivity but discuss below when this may affect our model accuracy (Assumption 2). Further, we consider that the site response of any hillslope can be written as a constant average response over the whole landscape $\bar{S}$ plus a deviation term dS. Then,

$$P_{\mathrm{LSV}} = \alpha_V \left(\frac{b(\bar{S} + \mathrm{d}S)}{R} - a_c \right) \tag{2}$$

with R the distance between the source and the landscape cell of interest. Equation (2) cannot be solved because the spatial distribution of site effects, represented by dS, remains a major unknown. However, we are not trying to resolve the spatial distribution of landsliding but only the total volume caused by a point source, V_{ps}, that is the spatial integral of P_{LSV}. By definition $\int^{\theta}\int^{R} \mathrm{d}S(R,\theta)\mathrm{d}R\mathrm{d}\theta \to 0$ and we can neglect this term, giving

$$V_{ps} = \int^{\theta}\int^{R_H} P_{\mathrm{LSV}} R_H \mathrm{d}R_H \mathrm{d}\theta = \int^{\theta}\int^{R_H} \alpha_V \left(\frac{b\bar{S}}{R} - a_c \right) R_H dR_H \mathrm{d}\theta, \tag{3}$$

where R_H and θ are polar coordinates of any point at the surface above the projection of the seismic source at a mean depth R_0, with R_H following $R^2 = R_0^2 + R_H^2$ (Figure 2). To progress, we consider an average landscape sensitivity $\bar{\alpha}_V$ and a constant shaking behavior in all directions (i.e., independent of θ) (Assumption 2), yielding

$$V_{ps} = 2\pi\bar{\alpha}_V \int_0^{R_{\mathrm{HMAX}}} \left(\frac{b\bar{S}}{\sqrt{R_0^2 + R_H^2}} - a_c \right) R_H \mathrm{d}R_H, \tag{4}$$

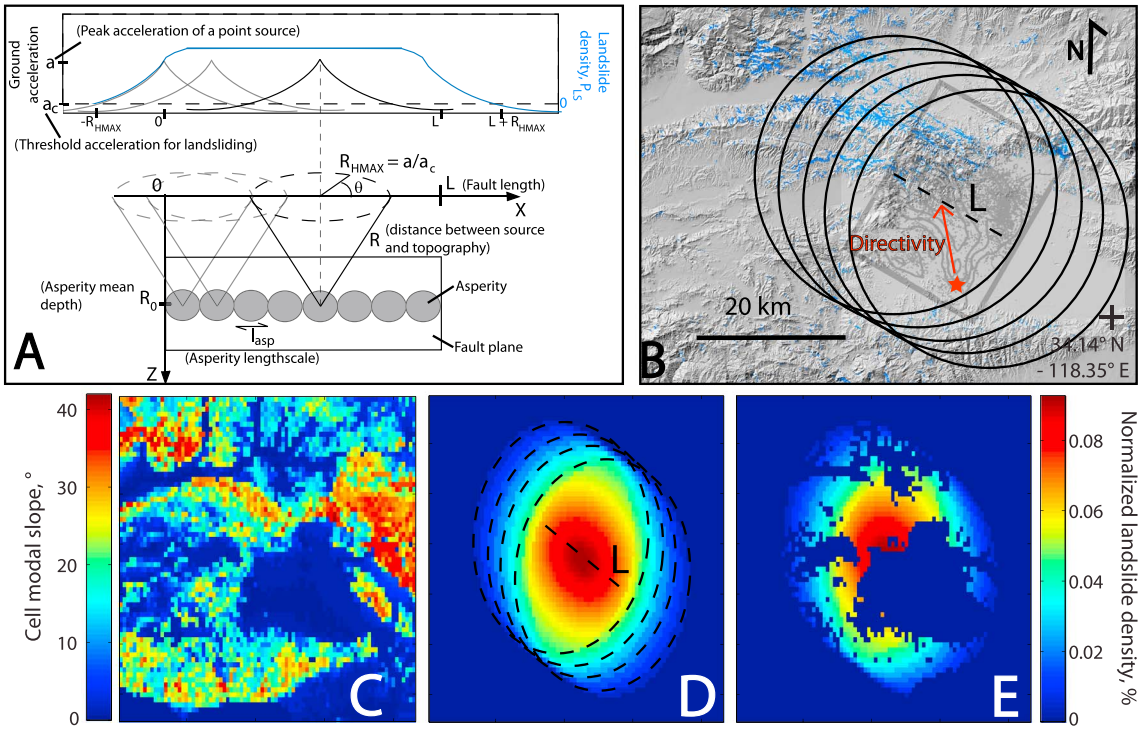

Figure 2. (a) Sketch of the geometry and relevant variables to describe the emission of seismic waves along a fault and their effect at the surface. (b) Example of digital elevation model hillshade of the area affected by the 1994, M_w 6.6 Northridge earthquake. Triggered landslides are shown in blue [*Harp and Jibson*, 1996]. The fault plane with slip contours and aftershocks is shown in black (modified from *Wald et al.* [1996]). Multiple black circles represent areas affected by seismic waves emitted by sources along the fault, from which the surface projection is shown with a dashed black line. (c) Modal slope map of the landscape affected by the 1994 Northridge earthquake, subdivided in 1 km^2 cells. (d) Idealized shaking map converted into a normalized landslide density. Sources and their effect on the surface, identical to Figures 2a and 2b are shown in black. (e) Remaining normalized landslide density after setting all cells with a modal slope <8° to zero. The sum of all cell values of this map is between 0 and 1 and represents A_{topo}, a first-order correction for topographic availability. This is only first order as the actual shaking map may be much more complex than the idealized representation in Figure 2d. For example, in the particular case of Northrige, the directivity must have amplified the shaking to the north, meaning that the flatlands to the south did not limit landsliding as much as our simplification assumes.

where R_{HMAX} is the horizontal distance from the wave source at which we expect the landsliding to end because the shaking drops below a_c, that is, $R_{HMAX} = \sqrt{(b.\bar{S}/a_c)^2 - R_0^2}$. It is important to note that because we neglected the spatial variability of site effects (dS), that modulate the ground shaking, and of hillslope properties, that affects the slope sensitivity to shaking (α), our model does not retain any spatial information and only predicts a bulk landslide volume or area over the whole affected landscape. Integrating, we obtain:

$$V_{ps} = \pi \bar{\alpha}_V a_c R_0^2 \left(\frac{b\bar{S}}{R_0 a_c} - 1 \right)^2. \quad (5)$$

Up to this point, only the ground shaking that a landscape would experience for a single point source of wave emission has been considered. However, during an earthquake waves are emitted as the rupture propagates along the fault length, L, and multiple sources, at a mean depth $\bar{R}_0$, will shake the landscape over an extended area, emitting multiple wave trains that will contribute to landsliding on a given hillslope [*Meunier et al.*, 2013]. The simplest model representing this considers that the total landslide volume for the whole fault, V_p, is the linear sum of all point sources along the fault, that is, $V_p = N_{ps}.V_{ps}$, with N_{ps} the number of sources (Figure 2a). N_{ps} cannot be constrained easily but it must scale at first order with the fault length L along which the rupture propagates and then with parameters such as the rupture velocity and the antecedent stress distribution on the fault. Full representation of these effects is out of the scope of our study and instead we assume that the number of point sources is the number of asperities where high-frequency waves are emitted, leading to

$$V_p = V_{ps}.N_{ps} = \pi \bar{\alpha}_V a_c \bar{R}_0^2 \left(\frac{b\bar{S}}{\bar{R}_0 a_c} - 1 \right)^2 \frac{L}{l_{asp}} \quad (6)$$

with l_{asp} the characteristic length of an asperity. Our approach considers the summed effect of multiple wave trains, which is equivalent to a shaking duration in the sense that ground shaking is applied several times on the landscape. Note, however, that sites are assumed to respond linearly, meaning that the possibility of material weakening or strengthening due to prolonged strong ground motion is ignored. Our approach ignores secondary effects that modulate shaking duration at a site, such as the source-site distance or resonance effects due to sedimentary layers [*Kempton and Stewart*, 2006]. Nevertheless, duration increases with $Mo^{1/3}$ [*Kempton and Stewart*, 2006], similar to the scaling of L/l_{asp} with $Mo^{2/5}$ (cf. equation (7)), suggesting that most of the duration increase associated with moment is captured by our model. Because the areal landslide density P_{LSA} also scales with $a - a_c$, our prediction for the total area of landslide A_p would have exactly the same form as equations (5) and (6) but with a different landscape sensitivity term $\bar{\alpha}_A$. The parameter $\bar{S}$ is included to be consistent with current understanding of ground shaking but cannot be constrained in this paper and is therefore assumed to be constant. Neglecting the spatial variability of site effects, dS, and of geomorphic sensitivity, α, as well as directivity of seismic waves are operational requirements that add potentially significant uncertainties to our prediction and these factors represent important challenges for future work. Hence, the model inputs are R_0, to be estimated for each earthquake, a_c, taken to be around 0.15 (cf. previous discussion after equation (1)), L and b, varying mainly with the seismic moment, and $\bar{\alpha}_V$, varying with substrate strength, local topographic gradient and conditioning factors such as antecedent rain, and requiring empirical constraints.

The most up to date scaling relation between L and Mo [*Leonard*, 2010] states that

$$L = \frac{Mo^{2/5}}{\mu C_1^{3/2} C_2} \tag{7}$$

with μ the shear modulus, assumed to be 3.3 GPa and $C_1 = 16.5\ \mathrm{m}^{1/3}$ and $C_2 = 3.7.10^{-5}$ constants derived empirically from many earthquakes [*Leonard*, 2010]. This scaling holds for fault lengths of about 3.5 km to 225 km for thrust earthquakes of M_w 5 to 8. Therefore, we assume that $l_{asp} = 3$ km, yielding 1 to 75 asperities or point sources for earthquakes in this magnitude range. Note that because we assume a uniform l_{asp} for all earthquakes, a different value would not change any of the results of our studies apart from the numerical value of the material sensitivity (cf. equation (11)).

Strike-slip earthquakes need to be considered separately. When they reach a critical seismic moment, Mo^*, then their fault width reaches the size of the seismogenic layer. After this, fault width cannot grow and the scaling becomes

$$\forall Mo > Mo^*, \qquad L = \frac{Mo^{2/3}}{\mu C_1^{3/2}.H_s} \tag{8}$$

with the seismogenic layer thickness assumed constant $H_s = 17$ km [*Leonard*, 2010].

For the inferred source acceleration at a given frequency, b, we use the scaling relation proposed by *Boore and Atkinson* [2008]:

$$b = b_{sat} \exp\left(e_5(M_w - M_h) + e_6(M_w - M_h)^2\right) \tag{9}$$

$$\forall M_w > M_h, \qquad b = b_{sat} \exp\left(e_7(M_w - M_h)\right), \tag{10}$$

where M_w is the moment magnitude, $M_h = 6.75$ a hinge magnitude above which the acceleration carried by seismic waves saturates at b_{sat}, and $e_5 = 0.6728$, $e_6 = -0.1826$, and $e_7 = 0.054$ are constants for 1 Hz waves. These constants were determined empirically from records of 58 earthquakes for a wide range of frequencies [*Boore and Atkinson*, 2008]. We focus on the 1 Hz frequency, because we consider it most appropriate for landslide triggering (Assumption 3). Earthquake magnitude is derived from the moment based on the empirical relationship $M_w = 2/3(\log Mo - 9.1)$ [*Hanks and Kanamori*, 1979].This relationship is consistent with theoretical predictions based on earthquake emission spectra and attenuation [*Baltay and Hanks*, 2014]. For earthquakes larger than $M_w \sim 6.8$ with numerous strong motion measurements, $b_{sat}.\bar{S}$ can be related to the epicentral ground acceleration a, with $a = b.\bar{S}/R_0$. However, only a few of the earthquakes in our database were large enough and sufficiently well instrumented for this approach. Hence, we chose $b_{sat}.\bar{S} = 4000$ m, meaning that large earthquakes with a shallow source depth of 5–10 km would have mean peak ground acceleration (PGA) above asperities of 0.4–0.8, ignoring ground shaking modulation due to site effects.

This is consistent with strong motion measurements from the 1999 Chi-Chi (Taiwan) and 2008 Sichuan (China) earthquakes [*Lee et al.*, 2001; *Li et al.*, 2008].

A further consideration is that different types of earthquake focal mechanisms normally give rise to different ground motion, due to interactions between fault geometry and the free surface [*Oglesby et al.*, 2000]. Based on ground motion measurements, *Boore and Atkinson* [2008] have proposed similar b for strike slip and reverse fault mechanisms but 30% smaller b for normal faulting. Consequently, we prescribe $b_{sat}.\bar{S} = 2800$ m for normal fault earthquakes.

In our model, then, the critical moment, above which V_p assumes a nonzero value is modulated by R_0 and ranges between 10^{16} and 10^{19} N m (Figure 1b). Above this critical moment, V_p rises sharply, driven by the exponential increase of the source acceleration (b) with increasing earthquake moment (equation (9)). After reaching the hinge magnitude, $M_h = 6.75$, the acceleration term saturates and V_p is primarily increasing due to fault length (L) growth with moment. Therefore, for these large events V_p is scaling as a power law of the moment, with an exponent of two fifths for dip-slip events, and an exponent of two thirds for strike-slip events (equations (7) and (8)). These exponent values are much less than the exponent value of 1 or 3/2 obtained through direct fitting of a power law to the earthquake moment and landslide volume data (Figure 1). In the case of earthquake sequences in which earthquakes preceding or following the main shock have more than 30% of the main shock moment, we can compute and sum the associated landsliding of all events, neglecting any possible effects of transient preconditioning of the landscape [*Marc et al.*, 2015]. This was done for the 1980 Mammoth Lake (USA), the 1993 Finisterre (Papua New Guinea, PNG), the 1997 Umbria-Marche (Italy), the 2002 Aysen (Chile), and the 2004 Niigata (Japan) earthquake sequences and the moment and depth of the subevents are reported in Table S1.

3.2. Consequences of Model Assumptions

Three important assumptions enable a simple analytical solution of our model. The relevance and associated uncertainties of these assumptions are explored, briefly, in turn.

Assumption 1 is that geometrical spreading is dominant over inelastic attenuation. For S waves with frequency $f = 1$ Hz (cf. Assumption 3) and velocity $V_s \sim 3$ km s^{-1}, the inelastic attenuation at a distance R, is $\exp(-\pi fR/qV_s)$, with q the quality factor, typically ~100 in the upper crust [*Wallace and Lay*, 1995]. Therefore, at 10 km, 20 km, and 25 km the attenuation would reduce the shaking by about 10%, 19%, and 23%, respectively. The integrated effect over a larger earthquake area would be somewhere within this range. Neglecting this effect causes overestimation of the predicted total landslide volume V_p by about 15–20%, depending on the local q. In view of other sources of uncertainty in the model, neglecting inelastic attenuation seems practical and reasonable.

Assumption 2 is that we can use an average topographic sensitivity relevant for the landscape over the whole fault length. The topographic sensitivity may be relatively homogeneous in steep mountainous terrain with moderately uniform lithology, topography, and climate, but not for events near coastlines (2007 Aysen (Chile) or 2010 Haiti (Haiti)), or at a mountain front (2011 Lorca (Spain) or 2013 Lushan (China)). For such cases, we cannot easily assess whether the shaking was equally distributed between flat and steep areas, and therefore, we must ignore this complexity. However, it is possible to anticipate the amount of missing landsliding due to insufficient topographic steepness, i.e., areas where α_V tends to zero. Therefore, we subdivide the total area where shaking exceeded the critical acceleration into a zone of flat land where the modal value of the topographic slope distribution is below 8° and not likely prone to failure and a zone where hillslopes are more likely to be sufficiently steep for landsliding to occur. We chose a modal slope of 8° because almost no earthquake-triggered landslides have been detected on slopes below 8–12° [*Parise and Jibson*, 2000; *Lin et al.*, 2008; *Gorum et al.*, 2013]. In our calculations of local slope gradients, we have consistently used the 30 m Aster Global Digital Elevation Model (GDEM), which pairs a relatively high resolution with global coverage, to obtain comparable characterizations of the epicentral topographies for all cases in our catalog. For a given landscape and earthquake, we have computed the slope gradient distribution within 1 km^2 cells (i.e., $33 \times 33 = 1089$ pixels) above the fault and the expected P_{LS} pattern, knowing L, R_0, and b (Figure 2). This pattern is a first-order approximation that neglects directivity and site effects and therefore not necessarily suited to the prediction of landslide spatial distribution. However, it allows computation of the total percentage of V_p expected in sufficiently steep cells. This fraction is named A_{topo} (Figure 2). We note that using 6° or 10° as a threshold would change A_{topo} by less than 5% in most cases. Multiplying the total landslide volume obtained from equation (6) by A_{topo} then yields a volume adjusted for the available topography. For very

simple topography, A_{topo} can also be estimated safely based on symmetry (e.g., for coastal area or fault bounded topography $A_{topo} \sim 0.5$). This correction will fail if strong directivity effects apply. However, we note that when A_{topo} is close to one (>50% of our events) and the earthquake area has steep slopes in all directions, directivity is not likely to change the total landslide volume, unless a strong anisotropy in rock mass strength is aligned with the directivity. Given that significant directivity effects are not normally systematic on regional scales, we do not expect any general directivity-related bias, although it may affect the prediction of some cases, such as the 1994 Northridge (USA) earthquake (Figure 2). This correction will fail if strong directivity effects are present. However, we note that when A_{topo} is close to one (>50% of our cases, Table S1), meaning that steep slopes abound, directivity is not likely to change the total landslide volume, unless a strong anisotropy in rock mass strength exists and is aligned with the directivity. Further taking into account that significant directivity effects are not systematic, we do not expect a general bias related to directivity, although it can affect the prediction of some events, such as the 1994 Northridge (USA) earthquake (cf. Figure 2 and discussion in section 5.1.3).

Assumption 3 is that the most relevant seismic waves for landslide triggering are *S* waves with a frequency of about 1 Hz. For intermediate size earthquakes, landsliding is most intense at the epicenter [*Meunier et al.*, 2007], where surface waves have not yet formed. This implies that body waves and therefore *S* waves with larger accelerations are the dominant landslide trigger. In larger earthquakes, surface waves may play a more important role in landslide triggering and neglecting them may cause the model to underpredict total landsliding. The exact frequency range over which landslides are efficiently triggered is difficult to constrain precisely but can be bracketed. Very high-frequency waves, >10 Hz would loose energy due to inelastic attenuation that would prevent landslide triggering at distances of 15–20 km or more from the source, contrary to common observations. On the other hand, low frequency waves at 0.1 Hz are unlikely to trigger landslides because shallow *S* waves with a velocity of about 500–800 m s^{-1} [e.g., *Picozzi et al.*, 2005] have wavelengths of 5–8 km, too large to cause damage in hillslopes with length scales of 100–500 m. Observations of landslide clustering on ridge crests where optimal topographic amplification of seismic waves is at about 1 Hz lend direct observational support to our assumption [*Meunier et al.*, 2008]. In any case, the exact frequency band for landslide triggering is not a strict requirement and we have modeled our source term (equations (9) and (10)) for different frequencies (see section 5).

3.3. Model Uncertainties

Our model requires precise knowledge of the seismic moment and source depth of an earthquake. For these parameters, we estimated a most likely value with a range of possible values. Without information on the uncertainty function we assumed it to be normal, implying that the estimated range of values represents a $2-\sigma$ range. It is assumed that the other model parameters, that is, the rupture velocity, critical acceleration, saturation acceleration, and hinge magnitude, have independent normal distributions with mean and standard deviation of 2000 ± 200 m/s, 0.15 ± 0.02, 4000 ± 400 m and 6.75 ± 0.1, respectively. We performed a Monte-Carlo simulation sampling 50,000 times for each parameter distribution and built a distribution of the predicted total landslide volume. This allowed us to constrain how the predicted volumes vary with the model parameters and with moment and depth uncertainties (Figure S4). As the resulting landslide volume distributions are often strongly skewed, specification of a mean and standard deviation is not meaningful. Instead we used a percentile description, with the 25th, 50th, and 75th percentile as our minimum, preferred and maximum prediction.

4. Landscape Sensitivity

We compare the general pattern of the volume estimates from landslide inventories with the model behavior, assuming $\alpha_V = 0.05$, for a thrust fault with a mean asperity depth of 10 km and a rugged topography with $A_{topo} = 1$. Model results for this specification intersect the bulk of our data within uncertainty (Figure 1b). Runs with shallower or deeper sources, at 3 or 20 km, predict total landslide volumes that bracket most of the estimates in our database. However, on closer inspection many individual data points do not lie near to their equivalent model depth curve (Figure 1b). It is clear that the landscape sensitivity term α, in which geomorphic variables such as slope, strength, and pore pressure have been bundled, cannot be kept constant. Quantitative controls on α are hard to derive theoretically. Therefore, we opted for an empirical approach. With no or very limited information about rock strength and antecedent moisture for most cases we start by constraining the dependency of the sensitivity term on the distribution of local slope gradients.

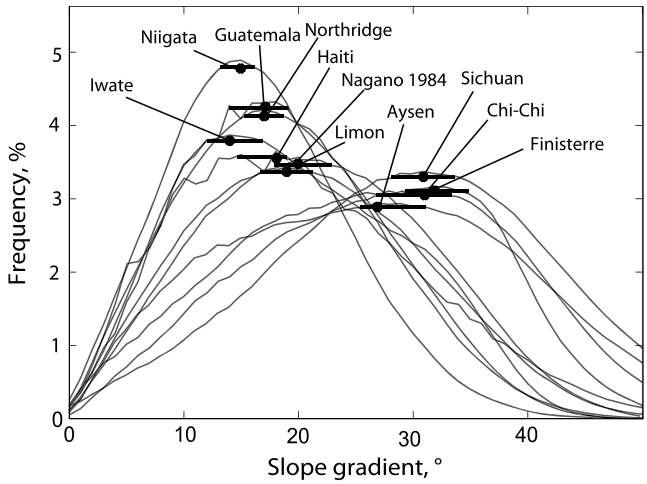

Figure 3. Probability distribution of local topographic slopes in the epicentral areas of the 11 earthquakes with comprehensive landslide inventories. Black dots and bars show the modal slopes with an uncertainty range set arbitrarily at 98% of the modal frequency. The remaining distributions of our database are shown in Figure S5. After removal of localized flat plains, all areas have unimodal slope distributions, but with diverse kurtosis or skewness.

4.1. Topographic Steepness

In order to constrain the effect of topographic slope on the sensitivity of an entire landscape to seismic perturbation, we used first-order statistical indicators of slope distribution. Slopes vary across upland landscapes, often with a unimodal probability distribution [*Wolinsky and Pratson*, 2005; *Lin et al.*, 2008; *Gorum et al.*, 2013] in which the most common, or modal slope is a relevant measure of the landscape steepness. For each earthquake, we extracted a slope histogram from the 30 m Aster GDEM for the area where our model predicted significant earthquake-triggered landsliding. This corresponds to the area used to determine A_{topo}, excluding any flat valley floors (i.e., cells with modal slope <8°) (Figures 3 and S5). Against this modal slope, we plotted the estimated total volume of landslides triggered by an earthquake divided by the volume predicted by the model, corrected for the available topography. Results are shown in Figure 4, where horizontal whiskers represent an arbitrary measure of steepness uncertainty given by the range of slopes reaching 98% of the modal frequency (Figure 3). Landslide volumes are predicted approximately correct for topographies with modal slope $S_{\text{mod}} \sim 35°$, but overpredicted for gentler topographies, up to 50-fold for landscapes with $S_{\text{mod}} \sim 12°$ (Figure 4). A general reduction of landslide incidence with decreasing landscape steepness is expected and explains much of our data. Eleven cases (1980 Friuli (Italy), 1987 Umbria (Italy), 1994 Arthur's Pass (New Zealand), 2002 Avaj (Iran), 2002 Denali (USA), 2004 Rotoehu (New Zealand), 2009 L'Aquila (Italy), 2010 Cucapah (Mexico), 2010 Yushu (China), 2011 Lorca (Spain), and 2011 Nagano (Japan)) remain as outliers compared to the broad trend defined by the residual data (Figure 4). This is not a surprise, as the landscape sensitivity must also depend on the geomechanical strength and hydrological saturation state of its hillslopes. Outliers may have a distinct hillslope strength or seismological specificities and we will discuss them later. Note that cases without source depth constraints, the 1957 Daly City (USA), 1950 Assam (India), and 1855 Wairapa (New Zealand) earthquakes, were not considered, because it is not meaningful to deduce the effects of steepness based on residuals that do not have good first-order constraints. We assume that those cases within one standard deviation of our least squares regression between modal slope and the logarithm of the predicted total landslide volume over the estimated total volume, S_{mod} versus $\log(V_p/V)$, are adequately described by an average rock strength and moisture content, whatever that may be. Notably, the exponential function defined by those cases ($R^2 = 0.62$, $N = 26$) has a very similar trend to the equivalent one defined by our 11 best constrained inventories ($R^2 = 0.67$, $N = 11$, Figure 4). Therefore, we can express the landscape sensitivity as a function of the landscape modal slope:

$$\forall b.\bar{S} > a_c R_0, V_p^s = \pi \bar{\delta}_V a_c R_0^2 \left(\frac{b\bar{S}}{R_0 a_c} - 1 \right)^2 \frac{L}{l_{\text{asp}}} \exp\left(\frac{S_{\text{mod}}}{T_{\text{SV}}} \right) A_{\text{topo}}, \tag{11}$$

where $\bar{\delta}_V$ is an average material sensitivity term independent of slope geometry, but still incorporating the effects of rock strength and wetness of the landscape, and T_{SV} is a steepness scaling constant. $\bar{\delta}_V$ and T_{SV} were

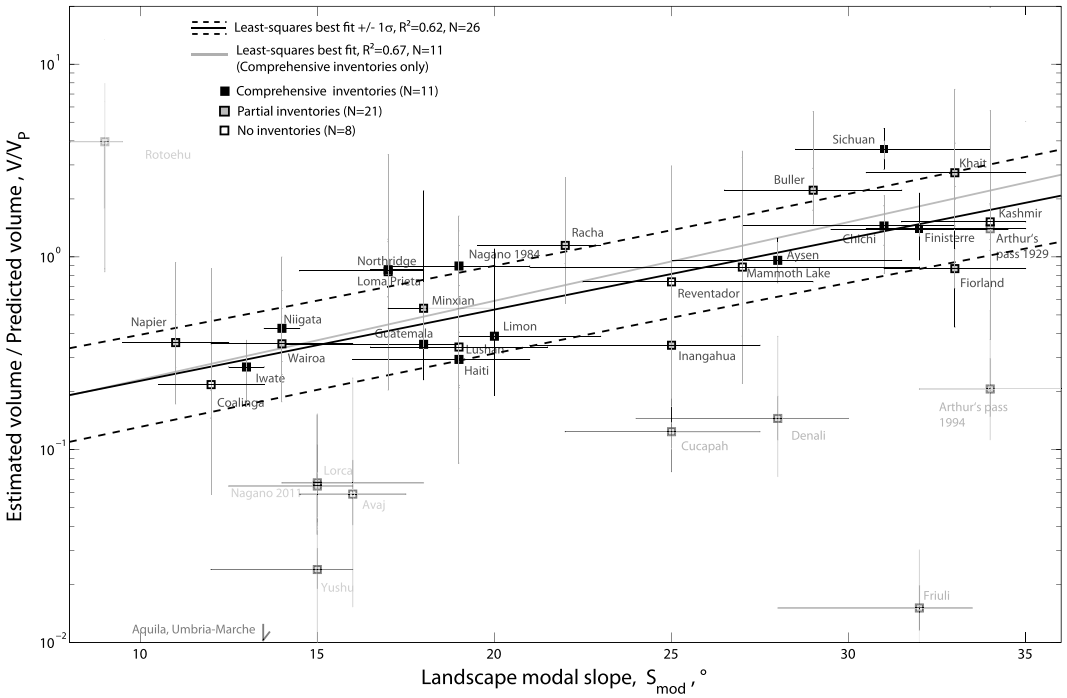

Figure 4. Ratio of the estimated and predicted total volume of triggered landslides plotted against landscape modal slope for all events with sufficient data (i.e., excluding the 1950 Assam (India), 1957 Daly City (USA), and 1855 Wairapa (NZ) earthquakes) ($N = 37$). The largely overpredicted Italian events (2009 Aquila and 1998 Umbria-Marche) (see Figure 6) plot outside of the frame. Gray and black bars represent the $2-\sigma$ uncertainties on the estimated volume for the preferred model and the 25–75th percentile of the distribution of model results against the mean estimated volume, respectively. Faded symbols are events excluded from the fit and assumed to have a different landscape sensitivity or seismological process from the bulk of our data (see discussion in section 5).

determined by orthogonal least squares minimization of the logarithm of the residuals against the modal slope values, yielding $\bar{\delta}_V = 4174 \pm 212\ \mathrm{m^3\ km^{-2}}$ and $T_{SV} = 11.6 \pm 0.6°$. This value of $\bar{\delta}_V$ can be taken to represent an average strength and pore pressure state of the fitted events. Apart from these two constants, every parameter in equation (11) has an unambiguous and distinct physical meaning, even if their value is sometimes, an average or mode of a broader distribution, and can be estimated for any earthquake scenario.

It must be emphasized that modal slope can only be a proxy for landscape sensitivity because most landslides associated with earthquakes occur at sites steeper than the modal slope of the landscape [*Parise and Jibson*, 2000; *Lin et al.*, 2008; *Gorum et al.*, 2013, 2014]. Implicit in this treatment is the assumption that the occurrence of steep slopes (e.g., >35°) scales with the modal slope. We performed the same analysis, using median instead of modal slope and obtained similar, but not better results.

4.2. Prediction of Total Area

The total area of landslides triggered by an earthquake must follow the same scaling with earthquake magnitude as landslide volume. However, α lumps the geomorphic controls on the probability of failure with those on the development and the final 3-D geometry of a landslide (see section 3.1). As processes setting landslide runout and width may not depend on slope, strength, or moisture in the same way than the ones setting landslide depth (for α_V only), we may expect a different dependency for $\bar{\alpha}_V$ and $\bar{\alpha}_A$. Initially, we chose a value $\bar{\alpha}_A = 0.05$, and compared our model predictions with 17 well-constrained cases. Fewer cases have well-constrained total landslide area, because this measure is less dominated by the largest landslides and therefore cannot be extrapolated based on a limited number of large landslides. Similar to landslide volume, the ratio of estimated over predicted landslide area is also positively correlated with the modal slope of the landscape (Figure 5a). Cases overpredicted (2002 Denali (USA), 2010 Yushu (China), or 2011 Nagano (Japan)) or underpredicted (1957 Daly City (USA)) in the volume domain (Figure 4) are likewise mispredicted in the area domain (Figure 5a). This is consistent with our interpretation that these events have a specific material

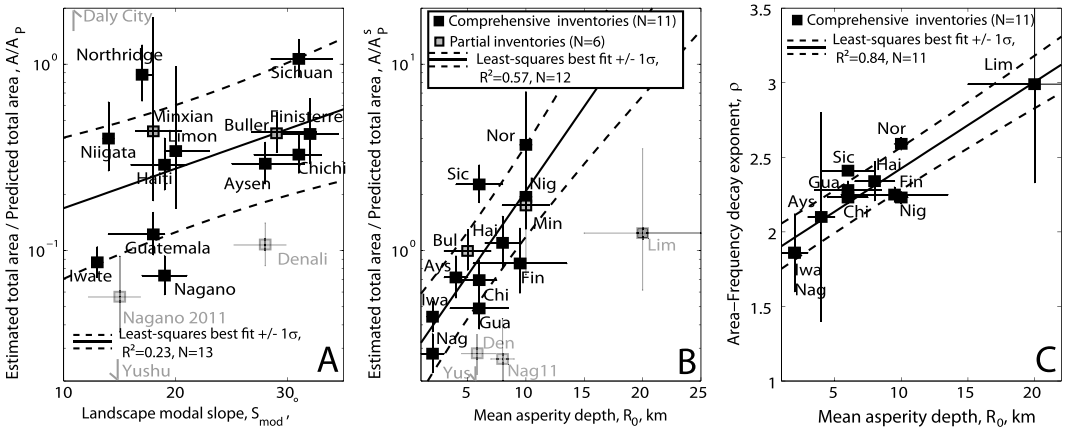

Figure 5. (a) Ratio of the estimated and predicted total area of triggered landslides plotted against landscape modal slope for all events with sufficient data ($N = 17$). (b) Ratio of the estimated and predicted total landslide area divided by the empirical slope correction from the left panel, plotted against the mean asperity depth R_0. Here the 1991 Limon earthquake was excluded from the fit because its estimate of A is artificially low due to resolution censoring of the small landslides. (c) Power law decay exponent ρ of the landslide area-frequency distribution of our 11 comprehensive inventories (see Figure S10) plotted against the mean asperity depth R_0. In Figures 5a and 5b y error bars represent model result uncertainties, that is 25–75th percentile of the distribution of model results. The 1957 Daly City (USA), the 2010 Yushu (China), the 2002 Denali (USA), and the 2011 Nagano were excluded from the fits shown in Figures 5a and 5b, because they likely violate key model assumptions or have a specific material sensitivity (see section 5.1.4).

sensitivity and/or violate our seismological assumptions, and we have ignored them when determining the best fit sensitivity constants in our total area prediction:

$$\forall b\bar{S} > a_c R_0, \qquad A_p^s = \pi \bar{\delta}_A a_c R_0^2 \left(\frac{b\bar{S}}{R_0 a_c} - 1 \right)^2 \frac{L}{l_{\text{asp}}} \exp\left(\frac{S_{\text{mod}}}{T_{\text{SA}}} \right) A_{\text{topo}} \tag{12}$$

with $\bar{\delta}_A$ and T_{SA} having a meaning analogous to $\bar{\delta}_V$ and T_{SV}. With an orthogonal least squares minimization of the logarithm of the residuals against the modal slope values, we obtained $\bar{\delta}_A = 3445 \pm 325$ m^2 km^{-2} and $T_{\text{SA}} = 15.8 \pm 1.5°$, indicating that topographic steepness is a lesser control on total landslide area than on total landslide volume. Even without the outliers, the best least squares exponential fit only accounts for about 20% of the variance ($R^2 = 0.23, N = 13$), further highlighting the limited control of landscape steepness on A. In the following discussion, we show that another parameter, related to the seismic source depth, is modulating A and is responsible for the poor variance reduction associated with landscape steepness. However, even if steepness appears a lesser control on landslide area than on volume, equation (12) yields predictions that are within a factor of 2 of the total area estimates for 11 out of 17 earthquakes (i.e., 65% success rate, Figure S6) and $R^2 = 0.73$.

5. Discussion

We derived expressions for the total volume and area of populations of earthquake-triggered landslides. These expressions aim to account for the principal characteristics of seismological and landsliding processes involved and thereby to improve the accuracy and robustness of predictions of total landslide volume and area for relevant earthquake scenarios. In the following, the accuracy of our expressions is compared to previous and current empirical relationships. Then we discuss the limitations of our model in accounting for landscape properties and seismological complexities for both the landslide volume and landslide area predictions. We end with examples of applications to well-constrained settings with recurring large earthquakes, the Alpine fault of the Southern Alps, New Zealand, and to the 2015 Gorkha earthquake in Nepal.

5.1. Strength and Limitations of our Prediction

5.1.1. Accuracy Compared to the Empirical Relationships

The relationship of *Keefer* [1994] and our empirical fit of earthquake-triggered landslide volume against moment have scatter of one to two orders of magnitude (Figure 1). Moreover, in both relations, predicted landslide volume increases more strongly with earthquake moment than in our model. Here we briefly consider the accuracy and insight gained through our seismologically consistent model compared to empirical approaches.

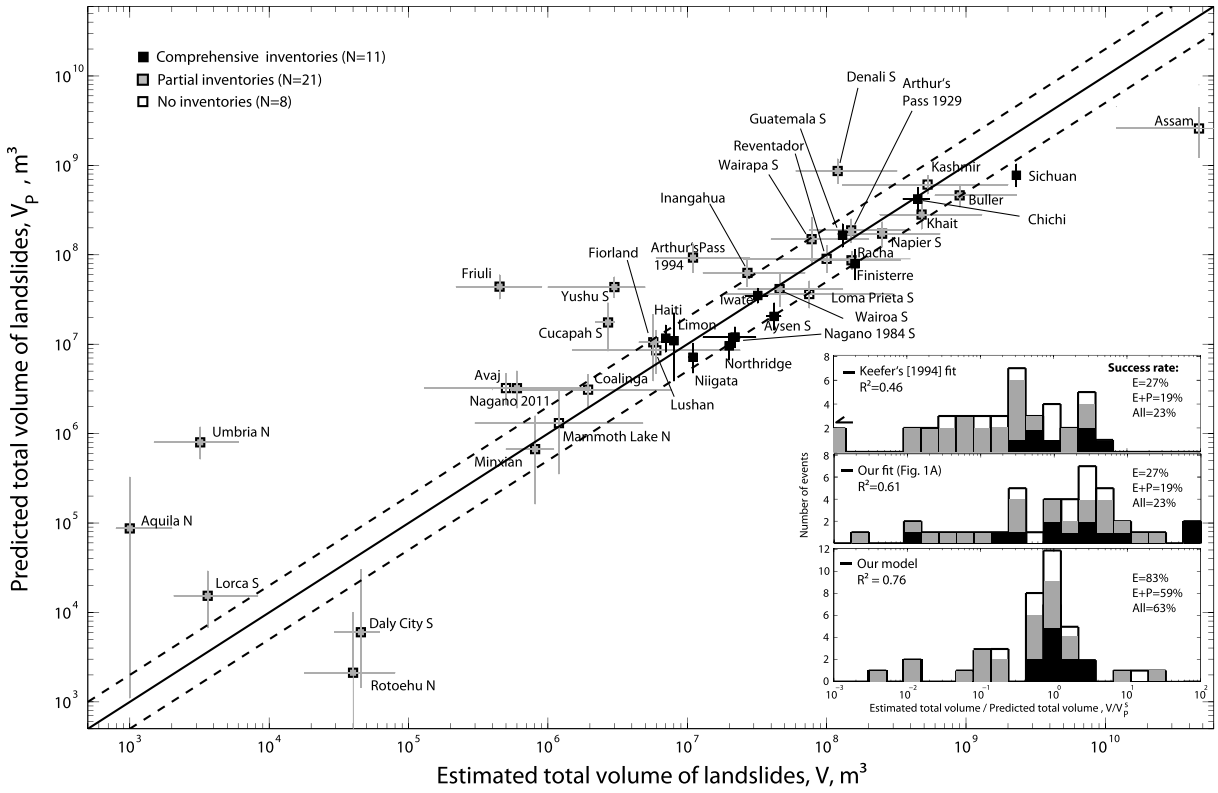

Figure 6. Predicted total landslide volume plotted against estimated total landslide volume for 40 earthquakes in our database (Table S1). For reference the one-one line, with a factor of 2 interval are shown as solid and dotted lines, respectively. Earthquakes on strikeslip or normal faults are indicated with (S) and (N) after the event name code. Inset: Histogram of the residuals of our model and the empirical fits of Figure 1. The black and gray fillings of the histograms refer to the number of comprehensive and partial inventories in each bin, respectively.

At the outset, it should be stressed that the landslide data used to test the accuracy of our model have diverse quality and uncertainties. Discrepancies between landslide volume estimates for poorly documented cases (1983 Coalinga (USA), 1980 Mammoth Lake (USA), 2002 Avaj (Iran), 1989 Loma Prieta (USA), 1987 Reventador (Ecuador), 2005 Kashmir (Pakistan), 2013 Lushan (China), and 1950 Assam (India)) and our model predictions may be due to inaccuracy of the published estimates as well as to the limitations of our model. Specifically, the landslide volume for the 1950 Assam earthquake was obtained using a constant landslide depth for all the perturbed areas, based on a few measurements only [*Mathur*, 1953]. The published volume for this case is therefore likely an overestimate, but it is harder to decipher the uncertainties of the other cases. Other events such as Daly City, Wairapa, or Rotoehu have relatively well constrained landslide volumes but lack detailed seismological information and are therefore hard to predict.

Using equation (11), we predict the landslide volume triggered by a given earthquake with greater accuracy than with the empirical fit defined from our extended database or than with the *Keefer* [1994] relationship (Figure 1). As 63% of model predictions are within a factor 2 of the corresponding volume estimate, compared to only 23% for both empirical fits (Figure 6). For the 11 best constrained inventories, this success rate improves to 82%, against 45% and 18% for the *Keefer* [1994] relationship and our empirical fit, respectively (Figure 6). Thus, our model represents a significant improvement on the accuracy of landslide volume predictions. Also of interest is the fact that larger differences between model predictions and volume estimates provide insight into those factors that also affect the landslide response to earthquakes but have not been adequately represented in our model. It appears that many discrepancies are due at least in part to an ill-constrained material sensitivity term, $\bar{\delta}_V$. The fact that the final residuals of our model, V/V_p^s, have no remaining correlation with earthquake moment nor with modal slope, mean asperity depth, or fault type (Figure S6), strengthens our assertion that these parameters have been properly accounted for, and that other parameters govern the outliers. Such parameters include seismological complexities, specific rock mass strength, or hydrological conditions.

We also tested wave acceleration emission constants, b (equation (9)), for different frequencies [*Boore and Atkinson*, 2008] and obtained similar, but not better results, for frequencies between 0.5 Hz and 3 Hz. However, frequency constants outside this range, such as $f = 0.25$ Hz or $f = 6$ Hz introduced a systematic bias with moment and much larger data misfits, supporting our assumption that frequencies of about 1 Hz are the most relevant for landslide triggering (Figure S7).

Finally, we assessed the effect of using hypocentral depth instead of the mean asperity depth for R_0 (Figure S8). For many earthquakes in our database, the difference between the hypocenter depth and the principal asperity depth is small, or assumed to be small. However, in 16 earthquakes considered here, the hypocenter was located substantially deeper than the asperity (Table S1). The attendant reduction of the predicted landslide volume in these cases degrade the correlation with the landscape modal slope (Figure S8) and the final accuracy of the model, supporting our decision to consider that asperities are the most important sources of seismic wave responsible for triggering of landslides.

5.1.2. Landscape Sensitivity and Rock Strength

Landscape sensitivity to seismic perturbation is set not only by the steepness and relief of the local topography but also by the geomechanical properties of the underlying soil and rock [*Hoek and Brown*, 1997; *Schmidt and Montgomery*, 1995]. In our model, this is represented by the material sensitivity, $\bar{\delta}_V$, which was kept constant in our treatment, even though it must vary with rock mass strength and could explain some outliers. Before addressing the outliers we note that with a constant material sensitivity, our model predicts total landslide volumes within a factor of 2 of estimated values in 25 cases in our catalog, that is, 63% (Figure 6), in spite of a large diversity of lithologies amongst these cases (Table S1). Antecedent rainfall is not accurately quantified, but amongst these 25 cases only a few had heavy rainfall or notable drought preceding the earthquake, suggesting that the average rock mass strength of the various landscapes must be similar. Fracturing and subsequent weathering, resulting from either tectonic or geomorphic drivers [*Molnar et al.*, 2007; *Clarke and Burbank*, 2010], are likely to have rendered a significant part of the landscape relatively weak [e.g., *Schmidt and Montgomery*, 1995] in the majority of our cases and independent of the lithology [*Gallen et al.*, 2015]. This does not preclude larger rock strength variations at the local scale from playing an important role in setting the spatial distribution of landslides [e.g., *Parise and Jibson*, 2000]. Three Italian earthquakes (1976 Friuli, 1997 Umbria-Marche, and 2009 L'Aquila), which occurred in terrain dominated by massive limestone cliffs, buck this trend. Landsliding due to these earthquakes was overpredicted by our model by two orders of magnitude, and consisted mainly of triggered rock falls and small rock avalanches [*Govi and Sorzana*, 1977; *Antonini et al.*, 2002; *Guzzetti et al.*, 2009], even though many other earthquakes of similar magnitude have solicited significant landsliding. This suggests that the hillslopes in the epicentral areas of the these Italian earthquakes had a much greater than average strength, possibly due to the relatively high cohesion of calcareous substrate. The 1991 Racha (Georgia) earthquake is the only other case with substantial limestone in the epicentral area. Its estimated landslide volume is very close to that predicted by the model (Figure 6), but the landslide volume was dominated by a few giant earthflows that occurred in slopes underlain by clay [*Jibson et al.*, 1994]. These flows make up two thirds of the total landslide volume, suggesting that weak response to shaking in limestone areas may have been compensated by more abundant landsliding in weaker, clay-rich substrates, coincidentally yielding a sum total landslide volume close to that predicted. In addition to the permanent effects of substrate quality, preconditioning of hillslope stability due to antecedent weather could also affect the sensitivity term. For most cases, the relevant meteorological information is lacking, but it is likely that many had some degree of substrate saturation and only some had exceptionally dry or wet conditions just before the earthquake. For example, the degree of hydrological saturation of hillslopes may have affected the 2002 Avaj (Iran) earthquake, which struck after prolonged drought. In this case large cracks in hillslopes, that could have become landslides in a wetter substrate, were widely observed [*Mahdavifar et al.*, 2006]. This may explain why the Avaj event is overpredicted by our model by a factor of 6. The 2010 Cucapah (Mexico) earthquake was also overpredicted by a factor of 6, possibly due to extremely dry conditions, although this case is difficult to evaluate because the topography above the 100 km long fault is very flat except for the narrow Sierra Cucapah (40 km long, 8 km wide) [*Wei et al.*, 2011], yielding $A_{\text{topo}} \sim 10\%$ and suggesting our assumption that site effects average out is likely violated. In contrast, very intense rainfall occurred less than a few days before the 1984 Nagano and 2004 Niigata (Japan), possibly causing these earthquakes to have a landslide volume 2 and 1.6 times larger than the model prediction, respectively.

5.1.3. Seismological Complexities

Besides substrate sensitivity, discrepancies between predicted and estimated landslide volumes may relate to seismological complexities or violation of the seismological assumptions in the model. This is most clearly demonstrated in cases that appear not to have been strongly affected by the substrate issues discussed in the previous section. There are seven events where specificities of the ground shaking, rather than anomalous rock strength or preconditioning, likely explain why documented and predicted landslide volumes differ by more than a factor of 4.

The 1957 Daly City (USA) and 2004 Rotoehu (NZ) cases had poorly constrained source depths with potentially major consequences for the predicted landslide volumes, as both earthquakes were close to the threshold for landslide triggering (M_w 5.3 and 5.4). In fact, for the range of mean asperity depths used, the 1957 Daly City (USA) earthquake should have produced between zero and half of the estimated landslide volume, according to our model. Additionally, these cases are difficult to evaluate because the earthquakes struck in mostly flat or submerged areas ($A_{topo} \sim 15-20\%$, with $S_{mod} = 10°$), with occasional oversteepened slopes on ocean or lake shores (>45°), where most landslides occurred [*Bonilla*, 1960; *Hancox et al.*, 2004]. In such cases, with only a small fraction of the topography steep enough for landsliding, our tenet that the mean shaking pattern is relevant and that the spatial pattern of site effects and directivity may be neglected is likely violated. In contrast, the 2010 Yushu (China) earthquake triggered about 7 times fewer landslides than expected from our model. The source depth of this earthquake is reasonably well constrained [*Sun et al.*, 2013] and we could not find strong evidence of specific preconditioning or an anomalous rock mass strength. However, seismological observations indicate that the rupture propagated at speeds in excess of the seismic shear wave velocity, with $v_r \sim 5$ km/s, that is, in supershear [*Wang and Mori*, 2012]. During the 2002 Denali (USA) earthquake, the third fault segment ruptured in supershear and was observed to emit fewer high-frequency waves than in subshear rupture [*Frankel*, 2004], with commensurately less attendant landsliding [*Gorum et al.*, 2014]. Thus, it is likely that these two earthquakes had less landsliding than our model predicted due to a reduction of high-frequency wave emission in supershear rupture. Supershear has not been reported for any other cases in the database, but we cannot exclude that some older cases may have had supershear ruptures that have remained unrecognized due to observational limitations.

The 2011 Nagano (Japan) earthquake induced about 5 times fewer landslides than expected from our model, possibly because the landscape was snow covered. This has been reported to damp ground shaking in numerical simulation [*McColl et al.*, 2012] and may also have played in the overprediction of landslide volume for the 2002 Denali earthquake. The volume of landslides triggered by the 2011 Lorca (Spain) and 1994 Arthur's Pass (New Zealand) were about 4 times and 8 times smaller than those predicted by our model, respectively. Both have reasonable depth constraints, on their epicenter at least, and especially dry conditions were not reported [*Hancox et al.*, 1997; *Alfaro et al.*, 2012]. The epicentral area of the Lorca earthquake comprises cliffs of strong limestones, but also slopes in weaker marls and slates, complicating any interpretation based on rock strength, while the 1929 Arthur's Pass case was adequately predicted with the average material sensitivity. For these cases, the volume mismatch remains unexplained. Discrepancies between predicted and estimated landslide volumes may also reflect some of the many aspects which have been overlooked in our model, such as strong local attenuation of seismic waves, seismic directivity or a geologic site effect pattern interacting with preferentially oriented topography, or specific seismic rupture processes affecting the relative importance of waves with 1–2 Hz frequencies. This is also true for the smaller volume discrepancies of some other events, for example, we note that the three well-constrained earthquake sequences (in Aysen, Niigata, and the Finisterre Range) are underpredicted by about a factor 2, possibly reflecting a heightened propensity to failure after the initial damage of the hillslopes. The 2010 Haiti earthquake mobilized only half the expected landslide volume, probably because almost the entire hanging wall of the seismogenic thrust was submerged and our topographic correction A_{topo} did not account for the fact that in addition to possible directivity effects, the strongest shaking usually occurs in the hanging wall of thrust faults rather than in the footwall [*Oglesby et al.*, 2000]. The directivity effect present during the 1994 Northridge (USA) earthquake certainly focused strong shaking and landsliding Northwest of the fault (Figure 2b) meaning that our $A_{topo} = 0.45$ correction should rather be $\sim 0.6 - 0.7$ if we were to impose a shift of the strong motion to the Northwest, reducing significantly the current underestimation of this event. However, such case-specific effects seem to be of limited importance for the majority of our examples.

5.1.4. Fault Style Influence on Earthquake-Triggered Landslides

Fault style has often been proposed to be a control on earthquake-triggered landsliding [e.g., *Tatard and Grasso*, 2013; *Gorum et al.*, 2014] and numerical models and observations suggest it affects ground shaking [*Oglesby et al.*, 2000]. Our treatment involves a 30% reduction of waves emitted by normal fault earthquakes [*Boore and Atkinson*, 2008], as compared to reverse or strike-slip mechanisms. It also assumes that large magnitude strike-slip earthquakes will occur on longer faults and induce more landslides (see equation (8)). We have explored the effects of these two hypotheses. Most of the normal fault events are difficult to evaluate not only because of their small magnitude but also because of specific lithological (1997 Umbria-Marche and 2009 L'Aquila) or topographic (2004 Rotoehu) constraints. Applying a reduction of shaking for normal faults, consistent with seismic observations [*Oglesby et al.*, 2000; *Boore and Atkinson*, 2008], may improve the model accuracy, but our landslide data are too scarce and noisy to support it. Nevertheless, if the 30% reduction in wave emission for normal faults is not applied, then the landslide volumes predicted by the model increase substantially, predicting correctly the 2004 Rotoehu (NZ) event, while the 1980 Mammoth Lake (USA) event, which was the only well-predicted normal fault case becomes substantially overpredicted (Figure S9). More well-constrained landslide inventories for normal fault earthquakes are needed to test this aspect of the model. Removing equation (8) from our treatment reduces the fit quality of residuals against modal slope and results in underprediction, by more than a factor of 2, of landslide volumes triggered by large strike-slip earthquakes such as the 1976 Guatemala and the 1931 Napier (NZ) earthquakes. However, our data do not support a major difference in earthquake-triggered landslide volume between strike-slip and reverse fault earthquakes (Figures 6 and S6). The same is true, in general, for integration of seismological complexities and sensitivity effects in our model and proper testing of predictions. The acquisition of high-quality landslide data for a larger number of earthquakes with different mechanisms remains an outstanding research challenge.

5.1.5. Total Landslide Area and Area-Frequency Distribution

Residuals for total landslide area, A/A_p^s, are similar to those for volume, with 11 out of 17 of all well-constrained inventories within a factor of 2, or 65% of success, 4 within a factor of 5 and 2 significant outliers (Figures 5b and S6). The estimated total landslide area, A is more sensitive to inclusion of small and intermediate size landslides ($<50,000$ m^2) than the total landslide volume. Low-mapping resolution may cause significant reduction of A, because many small landslides cannot be mapped confidently, as is clearly the case for our mapping of the 1991 Limon (Costa Rica) earthquake which is likely to have a total landslide area 2 to 3 times larger than the area used here. However, a lower resolution can also lead to an overestimation of the mapped area because disturbed areas may be blurred [*Marc and Hovius*, 2015]. Therefore, we cannot exclude that resolution effects may bias the older events in the database with a relatively low image quality, but it is unlikely to bias events mapped from high resolution imagery such as the 2004 Niigata, 1984 and 2011 Nagano, the 2008 Iwate, the 1976 Guatemala, and the 1994 Northridge earthquakes (Table S1). Notably, the area residuals appear to be correlated with the earthquake mean asperity depth ($R^2 = 0.58$, $N = 12$, Figure 5b), with the exception of the 1991 Limon event, for which A is underestimated, and the 1957 Daly City, the 2002 Denali, the 2010 Yushu, and the 2011 Nagano earthquakes for which the landslide volume prediction were poor. This trend is not visible for the volume residuals (Figure S6), suggesting that a process specific to small and intermediate size landslides, which are less important in setting the total landslide volume, is modulating the total area estimate. This is supported by the very strong correlation ($R^2 = 0.84$, $N = 11$, Figure 5b) between the mean asperity depth and the exponent ρ of the landslide area-frequency distribution for the 11 most comprehensive landslide inventories in this study (Figures 5c and S10). Note that here we included the Limon case because landslides smaller than $\sim$1000 m^2 that could not be mapped, do not affect the fit of the decay exponent. Thus, A is systematically underpredicted for deep earthquakes with a large number of small to medium size landslides relative to large landslides (large ρ), and A is consistently overpredicted for shallow earthquakes with relatively few small and medium size landslides. Because most of the 11 comprehensive inventories are for earthquakes at or above the hinge magnitude, $M_h = 6.75$, at which source term accelerations b saturate, ground shaking is decorrelated from seismic moment and primarily depends on wave attenuation and the mean asperity depth. Thus, correlation between ρ and depth supports the tenet that the relative abundance of small and large earthquake-triggered landslides is modulated by the shaking properties, consistent with observation on the spatial distribution of landslide size for single earthquakes [*Keefer and Manson*, 1998; *Khazai and Sitar*, 2004]. However, few mechanisms could explain a larger number of medium-sized landslide for deeper earthquakes, as the shaking intensity due to such earthquakes is likely to be lower. Possibly our description of attenuation is too conservative, but this would not explain why the attenuation model should

be different for the prediction of landslide volume and area. Alternatively, the shaking duration, which is not considered explicitly in our model, may be an important control on small-scale, shallow landsliding, whereas larger and deeper landslides may be primarily controlled by the shaking intensity. In this case the increase of shaking duration with earthquake source depth [*Kempton and Stewart*, 2006], that is, neglected in our model, may lead to the correlation we observe without affecting the predicted total landslide volume. Additional data are required to evaluate the effect of shaking duration and intensity on slope stability on specific length scales to be able and to better integrate these terms in our model framework.

5.2. Application to Earthquake Scenarios

Our model can be used when an earthquake is anticipated or after it has occurred. The seismic moment or the fault length, the mean asperity depth and the fault type may be specified based on paleo-earthquake information or initial seismological data. In either case, the active fault segment must be located, so that A_{topo} and the modal slope of the overlying area can be computed based on a 30 m digital elevation model (DEM), for consistency with our empirical correction for steepness (Figures 2 and 3). With these five quantities and their associated uncertainties, V_p and A_p and their uncertainties can be computed, using equations (11) and (12). Here two examples are explored briefly: the 2015 Gorkha earthquake in Nepal, for which preliminary seismological and geomorphological data are available at the time of writing [*Collins and Jibson*, 2015; *Kargel et al.*, 2015], but not yet a comprehensive landslide map, and an expected future large earthquake on the Alpine fault of New Zealand.

The M_w7.8 Gorkha earthquake, which occurred in April 2015, had an estimated seismic moment of 72.10^{19} N m and mean asperity depth of 15 ± 2 km [*Avouac et al.*, 2015]. From the available digital elevation data, we estimate $A_{\text{topo}} \sim 1$ and $S_{\text{mod}} = 33 \pm 2°$. With these constraints, our model predicts $V_p = 0.30(-0.11/+0.16)$ km^3. We assume that the affected area has a rock strength similar to that of the majority of the cases in our data base, but because the ground was very dry at the time of the rupture, propensity to failure of hillslopes may have been relatively low, so that the model prediction may be somewhat high, perhaps by a factor 2. Note that we used a slip distribution inversion to accurately locate the mean asperity depth. Such inversions can typically be performed some days or weeks after the earthquake, depending on the availability and processing of interferometric synthetic aperture radar, GPS, and strong motion data. However, a cruder landslide volume estimate could be made within 1 to 2 days after the earthquake, when first seismological constraints yielded similar moment estimates and a hypocentral depth between 15 and 25 km, leaving a wide range of possible mean asperity depths, between half the shallow hypocenter, at 8 km, and the deep hypocenter, at 25 km. With these initial constraints, the predicted total landslide volume was bracketed between 0.02 and 0.7 km^3.

Next, we consider the Alpine fault, bounding the Southern Alps of New Zealand to the west. This conspicuous tectonic feature has been shown to have consistently produced M_w8.1±0.1 earthquakes , every 330±30 years, over the last 8000 years [*Berryman et al.*, 2012]. The modal slope along the western Southern Alps is fairly constant, at about 32° [*Clarke and Burbank*, 2010], but decreases rapidly in the footwall of the fault, and as a representative slope we chose 30 ± 2°. The mean asperity depth where most of the wave emission is likely to occur cannot be predicted and is thus the major source of uncertainty. Instead of a single value, we can test two reasonable extremes for an earthquake of this size, 4 ± 1 and 8 ± 1 km. Along the ~300 km of the fault trace there are several sections where coastal plains or the sea lie within 20 km of the fault, leading to a 30% reduction of the total available area, mostly in the footwall of the fault, and a correction $A_{\text{topo}} \sim 85 \pm 5\%$. The shallow and deep earthquake scenarios yield predicted total landslide volumes of 1.0 $(-0.22/+0.28)$ km^3 and 0.7$(-0.17/+0.23)$ km^3 and total areas of 420$(-85/+105)$ km^2 and 290$(-70/+90)$ km^2, respectively. Our model does not provide any information about the spatial distribution of these landslides. However, it is safe to assume that the landslides will be distributed along the fault trace, with the highest density within a radius of ~20 km that means an area of about 1200 km^2. Hence, the average proportion of area affected by landslides along the fault is expected to be 2.4–3.5%. This bulk measure can be refined using various assumptions about the area likely to be affected more than average, based on local topographic steepness, or the expectation of stronger shaking in the hanging wall close to the fault [*Oglesby et al.*, 2000]. Coupled to a road or property density map such estimates may help to quantify risk due to triggered processes. The total landslide volume is likely to be a key factor responsible for seismically induced changes in weathering and fluvial chemistry [*Emberson et al.*, 2016; *Jin et al.*, 2015]. The total landslide area is crucial to evaluate the amount of standing biomass and soil biomass that will be harvested and may be buried, influencing the long term and short term carbon budget of the mountain belt [*Hilton et al.*, 2011]. Moreover, the total landslide volume can be converted into mean erosion rates over the recurrence intervals ($0.18 - 0.25$ mm yr^{-1}) and compared to

landslide erosion due to precipitation to assess the relative role of climate and seismicity in driving erosion in this setting [*Hovius et al.*, 1997]. Finally, as our model only requires DEM information and the prescription of the earthquake moment or fault length and depth, it can easily be integrated in landscape evolution models. This could enable assessment of the relative importance of earthquake erosion and the role of earthquakes in mountain building on longer time scales [*Li et al.*, 2014]. Beyond this, several issues are not addressed by our model, such as the precise location of the seismically triggered landslides, especially the larger ones that dominate the total landslide volume, the possible controls on the magnitude-frequency distribution of seismically triggered landslides, and the amount and timing of debris reaching the river network and the dynamics of its fluvial export.

6. Conclusion

We developed a seismologically consistent model relating the total volume and area of landslides triggered by an earthquake with the principal seismological characteristics of that earthquake and the main topographic attributes of the affected landscape. This model considers explicitly the effects of seismic moment, source depth, and rupture mechanism on triggered landsliding. It also incorporates the modulating influence of landscape steepness, here defined as the modal slope of the affected topography, on the amount of landsliding, constrained using an extensive database of 40 shallow continental earthquakes ranging between M_w 5.1 and M_w 8.6. However, variations of landscape sensitivity to seismic perturbation due to substrate strength remain elusive and have not been included in the model. This may be a cause of marked departures between predicted and estimated landslide volumes for some earthquakes in our database. However, model predictions are consistent with estimated total landslide volumes for a majority of events, although the precision of predictions is likely limited to a factor of 2 because of uncertainties on model input and simplifying assumptions. Predictions of total landslide area, with $R^2 = 0.73$ and 11 out of 17 events predicted within a factor of 2, appear to be less dependent on landscape steepness and may be affected by processes influencing the landslide area-frequency distribution, possibly the shaking duration. Nevertheless, our model significantly outperforms previous, empirical relations, with a successful prediction rate (i.e., prediction within a factor of 2 of estimate) of 63% against 23% and $R^2 = 0.76$ against $R^2 = 0.46$. It also predicts a very different scaling between landsliding and seismic moment for large earthquakes. Our model anticipates explicit representation of the role of earthquakes in landscape evolution models, reevaluation of seismically driven erosion fluxes, and useful application to risk analysis for earthquake scenarios. Further development of the model should include the introduction of quantitative rock strength proxies and the inclusion of more complex seismological processes, to achieve greater accuracy in predicting the total amount and spatial pattern of landsliding caused by earthquakes.

Notation

Symbols with a bar are average values for the whole fault or affected area (for example, $\bar{R}_0$, $\bar{\alpha}$ ...). All acceleration terms are normalized by the gravitational acceleration and therefore nondimensional.

a_c,	Threshold acceleration for ground damage ();
a,	Ground acceleration ();
A',V',	Individual landslide area or volume (m^2 or m^3);
A,V,	Estimated total landslide area or volume (m^2 or m^3);
A_p,V_p,	Predicted total landslide area or volume (m^2 or m^3);
A_p^s,V_p^s,	Predicted total landslide area or volume normalized for steepness (m^2 or m^3);
A_{topo},	Available topography corrector (%);
b,	Inferred acceleration due to waves at 1 km from the seismic source and a given frequency (m);
b_{sat},	Saturation acceleration for the scaling of b (m);
C_1,C_2,	Empirical constants for fault size scaling with moment [cf. *Leonard*, 2010];
e_5,e_6,e_7,	Empirical constants for b scaling with moment [cf. *Boore and Atkinson*, 2008];
f,	Seismic wave frequency (Hz);
H_s,	Seismogenic zone thickness (km);
L,	Fault plane length (km);
l_{asp},	Asperity length scale (km);
M_h,	Hinge magnitude above which b saturates ();
Mo,	Seismic moment (N m);

M_w, Moment magnitude ();
P_{LSA},P_{LSV}, Landslide area density (m^2 km^{-2}) and landslide volume density (m^3 km^{-2});
R, Distance between earthquake source and considered topography (km);
R_0, High-frequency waves source depth (i.e., mean asperity depth) (km);
R_H, Horizontal distance from the surface projection of the earthquake source (km);
R_{HMAX}, Maximal horizontal distance at which landsliding occur (km);
$\bar{S}$,dS, epicentral average and local deviation of the site effects amplification of a ();
S_{mod}, Modal slope of the affected hillslopes (i.e., affected topography excluding flat lands) (°);
T_{SV},T_{SA}, Empirical steepness constant for total volume and total area (°);
V_L, total volume of the largest landslides reported in incomplete inventories (m^3);
α_A,α_V, Landscape propensity to failure for acceleration exceeding a_c (m^2 km^{-2} or m^3 km^{-2});
δ_A,δ_V, Material propensity to failure (independent of slope geometry) (m^2 km^{-2} or m^3 km^{-2});
λ, γ, Empirical constants for area-volume scaling of landslides;
μ, Elastic shear modulus (Pa);
ρ, Landslide area-frequency distribution decay exponent (); and
θ, Angular coordinate (°).

Acknowledgments
OM is funded by a fellowship in the EU Marie Curie International Training Network TOPOMOD, project reference 264517. The authors have gratefully used Aster GDEM V2, a product of METI and NASA and Landsat imagery, made freely available by NASA. The authors thank Fausto Guzzetti and Francesca Ardizzone for their help in gathering landslide volume triggered by Italian earthquakes. The authors are very grateful to Kevin Schmidt, Noah Finnegan, and three anonymous reviewers for their very critical and constructive reviews that helped to clarify and improve this manuscript. O.M., N.H., and P.M. conceived the study and wrote the manuscript with input from the other authors. O.M. assembled and complemented the data base with help from T.U. and T.G., and performed all analyses, assisted by P.M. and N.H. Data that are not reported within the supporting information can be accessed by contacting the corresponding author. The authors have no conflicts of interest related to the work reported in this paper.

References

Abercrombie, R. E., T. H. Webb, R. Robinson, P. J. McGinty, J. J. Mori, and R. J. Beavan (2000), The enigma of the Arthur's Pass, New Zealand, earthquake: 1. Reconciling a variety of data for an unusual earthquake sequence, *J. Geophys. Res.*, *105*(B7), 16,119–16,137, doi:10.1029/2000JB900008.

Alfaro, P., J. Delgado, F. J. Garcia-Tortosa, L. Lenti, J. A. Lopez, C. Lopez-Casado, and S. Martino (2012), Widespread landslides induced by the M_w 5.1 earthquake of 11 May 2011 in Lorca, SE Spain, *Eng. Geol.*, *137–138*, 40–52, doi:10.1016/j.enggeo.2012.04.002.

Anderson, H., S. Beanland, G. Buck, D. Darby, G. Downes, J. Haines, J. Jackson, R. Robinson, and T. Webb (1994), The 1968 May 23 Inangahua, New Zealand, earthquake: An integrated geological, geodetic, and seismological source model, *N. Z. J. Geol. Geophys.*, *37*(1), 59–86, doi:10.1080/00288306.1994.9514601.

Antonini, G., F. Ardizzone, M. Cardinali, M. Galli, F. Guzzetti, and P. Reichenbach (2002), Surface deposits and landslide inventory map of the area affected by the 1997 Umbria-Marche earthquakes, *Boll. Soc. Geol. Ital.*, *121*(1), 843–853.

Avouac, J.-P., L. Meng, S. Wei, T. Wang, and J.-P. Ampuero (2015), Lower edge of locked Main Himalayan Thrust unzipped by the 2015 Gorkha earthquake, *Nat. Geosci.*, *8*, 708–711, doi:10.1038/ngeo2518.

Baltay, A. S., and T. C. Hanks (2014), Understanding the magnitude dependence of PGA and PGV in NGA West 2 data, *Bull. Seismol. Soc. Am.*, *104*(6), 2851–2865, doi:10.1785/0120130283.

Barlow, J., I. Barisin, N. Rosser, D. Petley, A. Densmore, and T. Wright (2015), Seismically-induced mass movements and volumetric fluxes resulting from the 2010 $M_w = 7.2$ earthquake in the Sierra Cucapah, Mexico, *Geomorphology*, *230*, 138–145, doi:10.1016/j.geomorph.2014.11.012.

Berryman, K., and P. Villamor (2004), Surface rupture of the Poulter Fault in the 1929 March 9 Arthur's Pass earthquake, and redefinition of the Kakapo Fault, New Zealand, *N. Z. J. Geol. Geophys.*, *47*(2), 341–351, doi:10.1080/00288306.2004.9515060.

Berryman, K. R., U. A. Cochran, K. J. Clark, G. P. Biasi, R. M. Langridge, and P. Villamor (2012), Major earthquakes occur regularly on an isolated plate boundary fault, *Science*, *336*(6089), 1690–1693, doi:10.1126/science.1218959.

Bird, J. F., and J. J. Bommer (2004), Earthquake losses due to ground failure, *Eng. Geol.*, *75*(2), 147–179, doi:10.1016/j.enggeo.2004.05.006.

Bonilla, M. G. (1960), Landslides in the San Francisco South quadrangle, California, *U.S. Geol. Surv. Open File Rep. 60-15*, U.S. Geol. Surv., Reston, Va.

Boore, D. M., and G. M. Atkinson (2008), Ground-motion prediction equations for the average horizontal component of PGA, PGV, and 5%-damped PSA at spectral periods between 0.01 s and 10.0 s, *Earthquake Spectra*, *24*(1), 99–138, doi:10.1193/1.2830434.

Cheloni, D., N. D'Agostino, E. D'Anastasio, and G. Selvaggi (2012), Reassessment of the source of the 1976 Friuli, NE Italy, earthquake sequence from the joint inversion of high-precision levelling and triangulation data, *Geophys. J. Int.*, *190*(2), 1279–1294, doi:10.1111/j.1365-246X.2012.05561.x.

Cirella, A., A. Piatanesi, M. Cocco, E. Tinti, L. Scognamiglio, A. Michelini, A. Lomax, and E. Boschi (2009), Rupture history of the 2009 L'Aquila (Italy) earthquake from non-linear joint inversion of strong motion and GPS data, *Geophys. Res. Lett.*, *36*, L19304, doi:10.1029/2009GL039795.

Clarke, B. A., and D. W. Burbank (2010), Bedrock fracturing, threshold hillslopes, and limits to the magnitude of bedrock landslides, *Earth Planet. Sci. Lett.*, *297*(3), 577–586.

Clough, R., and A. Chopra (1966), Earthquake stress analysis in Earth dams, *ASCE J. Eng. Mech. Div.*, *92*, 197–211.

Collins, B. D., and R. W. Jibson (2015), Assessment of existing and potential landslide hazards resulting from the April 25, 2015 Gorkha, Nepal earthquake sequence, *U.S. Geol. Surv. Open File Rep. 2015-1142*, U.S. Geol. Surv., Reston, Va.

Darby, D. J., and S. Beanland (1992), Possible source models for the 1855 Wairarapa earthquake, New Zealand, *J. Geophys. Res.*, *97*(B9), 12,375–12,389, doi:10.1029/92JB00567.

Doser, D. I., T. H. Webb, and D. E. Maunder (1999), Source parameters of large historical (1918-1962) earthquakes, South Island, New Zealand, *Geophys. J. Int.*, *139*(3), 769–794, doi:10.1046/j.1365-246x.1999.00986.x.

Dreyfus, D., E. M. Rathje, and R. W. Jibson (2013), The influence of different simplified sliding-block models and input parameters on regional predictions of seismic landslides triggered by the Northridge earthquake, *Eng. Geol.*, *163*, 41–54, doi:10.1016/j.enggeo.2013.05.015.

Elliott, J. L., J. T. Freymueller, and B. Rabus (2007), Coseismic deformation of the 2002 Denali Fault earthquake: Contributions from synthetic aperture radar range offsets, *J. Geophys. Res.*, *112*, B06421, doi:10.1029/2006JB004428.

Emberson, R., N. Hovius, A. Galy, and O. Marc (2016), Chemical weathering in active mountain belts controlled by stochastic bedrock landsliding, *Nat. Geosci.*, *9*, 42–45, doi:10.1038/ngeo2600.

Evans, S. G., N. J. Roberts, A. Ischuk, K. B. Delaney, G. S. Morozova, and O. Tutubalina (2009), Landslides triggered by the 1949 Khait earthquake, Tajikistan, and associated loss of life, *Eng. Geol.*, *109*(34), 195–212, doi:10.1016/j.enggeo.2009.08.007.

Fielding, E. J., A. Sladen, Z. Li, J.-P. Avouac, R. Burgmann, and I. Ryder (2013), Kinematic fault slip evolution source models of the 2008 M7.9 Wenchuan earthquake in China from SAR interferometry, GPS and teleseismic analysis and implications for Longmen Shan tectonics, *Geophys. J. Int.*, *194*, 1138–1166, doi:10.1093/gji/ggt155.

Frankel, A. (2004), Rupture process of the M 7.9 Denali fault, Alaska, earthquake: Subevents, directivity, and scaling of high-frequency ground motions, *Bull. Seismol. Soc. Am.*, *94*(6B), S234–S255, doi:10.1785/0120040612.

Gallen, S. F., M. K. Clark, and J. W. Godt (2015), Coseismic landslides reveal near-surface rock strength in a high-relief, tectonically active setting, *Geology*, *43*(1), 11–14, doi:10.1130/G36080.1.

Given, J. W., T. C. Wallace, and H. Kanamori (1982), Teleseismic analysis of the 1980 Mammoth Lakes earthquake sequence, *Bull. Seismol. Soc. Am.*, *72*(4), 1093–1109.

Goes, S. D. B., A. A. Velasco, S. Y. Schwartz, and T. Lay (1993), The April 22, 1991, Valle de la Estrella, Costa Rica ($M_w = 7.7$) earthquake and its tectonic implications: A broadband seismic study, *J. Geophys. Res.*, *98*(B5), 8127–8142, doi:10.1029/93JB00019.

Gorum, T., X. Fan, C. J. van Westen, R. Q. Huang, Q. Xu, C. Tang, and G. Wang (2011), Distribution pattern of earthquake-induced landslides triggered by the 12 May 2008 Wenchuan earthquake, *Geomorphology*, *133*(3), 152–167.

Gorum, T., C. J. van Westen, O. Korup, M. van der Meijde, X. Fan, and F. D. van der Meer (2013), Complex rupture mechanism and topography control symmetry of mass-wasting pattern, 2010 Haiti earthquake, *Geomorphology*, *184*, 127–138, doi:10.1016/j.geomorph.2012.11.027.

Gorum, T., O. Korup, C. J. van Westen, M. van der Meijde, C. Xu, and F. D. van der Meer (2014), Why so few? Landslides triggered by the 2002 Denali earthquake, Alaska, *Quat. Sci. Rev.*, *95*, 80–94, doi:10.1016/j.quascirev.2014.04.032.

Govi, M., and P. F. Sorzana (1977), Effetti geologici del terremoto: Frane, *Riv. Ital. Paleontol. Stratigr.*, *83*(2), 329–368.

Guzzetti, F., et al. (2009), Central Italy seismic sequences-induced landsliding: 1997-1998 Umbria Marche and 2008-2009 L'Aquila cases, in *Proceedings of the Conference: The Next Generation of Research on Earthquake-Induced Landslides: International Conference in Commemoration of 10th Anniversary of the Chi-Chi Earthquake, Taiwan*, edited by C.-T. Lee, pp. 52–61, Natl. Central Univ., Jhongli, Taiwan.

Hamzehloo, H. (2005), Strong ground motion modelling of causative fault for the 2002 Avaj earthquake, Iran, *Tectonophysics*, *409*(14), 159–174, doi:10.1016/j.tecto.2005.08.016.

Hancox, G., G. Perrin, and G. Dellow (1997), Earthquake-induced landsliding in New Zealand and implications for MM intensity and seismic hazard assessment, *GNS Client Rep. 43601B*, Inst. Geol. Nucl. Sci., Wellington.

Hancox, G., S. Cox, I. Turnbull, and M. Crozier (2003), Reconnaissance studies of landslides and other ground damage caused by the M_w 7.2 Fiordland earthquake of 22 August 2003, *Inst. Geol. Nucl. Sci. Rep. 2003/30*, Inst. Geol. Nucl. Sci., Wellington.

Hancox, G. T., G. Dellow, M. Mc Saveney, B. Scott, and P. Villamor (2004), Reconnaissance studies of landslides caused by the M_L 5.4 Lake Rotoehu earthquake and swarm of July 2004, *Inst. Geol. Nucl. Sci. Rep. 2004/24*, Inst. Geol. Nucl. Sci., Wellington.

Hanks, T. C., and H. Kanamori (1979), A moment magnitude scale, *J. Geophys. Res.*, *84*(B5), 2348–2350, doi:10.1029/JB084iB05p02348.

Harp, E., and R. Jibson (1996), Landslides triggered by the 1994 Northridge, California, earthquake, *Bull. Seismol. Soc. Am.*, *86*(1B), S319–S332.

Harp, E. L., and R. W. Jibson (2002), Anomalous concentrations of seismically triggered rock falls in Pacoima Canyon: Are they caused by highly susceptible slopes or local amplification of seismic shaking?, *Bull. Seismol. Soc. Am.*, *92*(8), 3180–3189, doi:10.1785/0120010171.

Harp, E. L., R. C. Wilson, and G. F. Wieczorek (1981), Landslides from the February 4, 1976, Guatemala earthquake, *U.S. Geol. Surv. Prof. Pap. 1204A*, U.S. Gov. Print. Off., Washington, D. C.

Harp, E. L., S. H. Hartzell, R. W. Jibson, L. Ramirez-Guzman, and R. G. Schmitt (2014), Relation of Landslides triggered by the kiholo bay earthquake to modeled ground motion, *Bull. Seismol. Soc. Am.*, *104*(5), 2529–2540, doi:10.1785/0120140047.

Has, B., T. Noro, K. Maruyama, A. Nakamura, K. Ogawa, and S. Onoda (2012), Characteristics of earthquake-induced landslides in a heavy snowfall region: Landslides triggered by the northern Nagano Prefecture earthquake, March 12, 2011, Japan, *Landslides*, *9*(4), 539–546, doi:10.1007/s10346-012-0344-6.

Hashimoto, M., Y. Fukushima, and Y. Fukahata (2011), Fan-delta uplift and mountain subsidence during the Haiti 2010 earthquake, *Nat. Geosci.*, *4*(4), 255–259, doi:10.1038/ngeo1115.

Hernandez, B., M. Cocco, F. Cotton, S. Stramondo, O. Scotti, F. Courboulex, and M. Campillo (2004), Rupture history of the 1997 Umbria-Marche (Central Italy) main shocks from the inversion of GPS, DInSAR and near field strong motion data, *Ann. Geophys.*, *47*(4), 1355–1376, doi:10.4401/ag-3349.

Hikima, K., and K. Koketsu (2005), Rupture processes of the 2004 Chuetsu (mid-Niigata prefecture) earthquake, Japan: A series of events in a complex fault system, *Geophys. Res. Lett.*, *32*, L18303, doi:10.1029/2005GL023588.

Hilton, R. G., P. Meunier, N. Hovius, P. J. Bellingham, and A. Galy (2011), Landslide impact on organic carbon cycling in a temperate montane forest, *Earth Surf. Processes Landforms*, *36*(12), 1670–1679, doi:10.1002/esp.2191.

Hoek, E., and E. T. Brown (1997), Practical estimates of rock mass strength, *Int. J. Rock Mech. Min. Sci.*, *34*(8), 1165–1186.

Hovius, N., and P. Meunier (2012), Earthquake ground motion and patterns of seismically induced landsliding, in *Landslides*, edited by J. J. Cleague and D. Stead, pp. 24–36, Cambridge Univ. Press, Cambridge, U. K.

Hovius, N., C. P. Stark, and P. A. Allen (1997), Sediment flux from a mountain belt derived by landslide mapping, *Geology*, *25*(3), 231–234, doi:10.1130/0091-7613(1997)025<0231:SFFAMB>2.3.CO;2.

Hovius, N., P. Meunier, C. Lin, H. Chen, Y. Chen, S. Dadson, M. Horng, and M. Lines (2011), Prolonged seismically induced erosion and the mass balance of a large earthquake, *Earth Planet. Sci. Lett.*, *304*(3), 347–355, doi:10.1016/j.epsl.2011.02.005.

Januzakov, K., M. Omuraliev, A. Omuralieva, B. Ilyasov, and V. Grebennikova (2003), *Strong Earthquakes of the Tien Shan (Within the Kyrgyzstan Territory and Adjacent Regions of the Countries of Central Asia)*, Ilim, Bishkek.

Jibson, R., and E. Harp (2006), Large rock avalanches triggered by the M 7.9 Denali Fault, Alaska, earthquake of 3 November 2002, *Eng. Geol.*, *83*, 144–160, doi:10.1016/j.enggeo.2005.06.029.

Jibson, R. W. (2011), Methods for assessing the stability of slopes during earthquakes—A retrospective, *Eng. Geol.*, *122*(12), 43–50, doi:10.1016/j.enggeo.2010.09.017.

Jibson, R. W., C. S. Prentice, B. A. Borissoff, E. A. Rogozhin, and C. J. Langer (1994), Some observations of landslides triggered by the 29 April 1991 Racha earthquake, Republic of Georgia, *Bull. Seismol. Soc. Am.*, *84*(4), 963–973.

Jin, Z., A. J. West, F. Zhang, Z. An, R. G. Hilton, J. Yu, J. Wang, G. Li, L. Deng, and X. Wang (2015), Seismically enhanced solute fluxes in the Yangtze River headwaters following the A.D. 2008 Wenchuan earthquake, *Geology*, *44*(1), 47–50, doi:10.1130/G37246.1.

Kargel, J. S., et al. (2015), Geomorphic and geologic controls of geohazards induced by Nepal's 2015 Gorkha earthquake, *Science*, *351*, aac8353, doi:10.1126/science.aac8353.

Kawakatsu, H., and G. P. Cadena (1991), Focal mechanisms of the March 6, 1987 Ecuador earthquakes, *J. Phys. Earth*, *39*(4), 589–597.

Keefer, D. K. (1984), Landslides caused by earthquakes, *Geol. Soc. Am. Bull.*, *95*(4), 406–421, doi:10.1130/0016-7606(1984)95<406:LCBE>2.0.CO;2.

Keefer, D. K. (1994), The importance of earthquake-induced landslides to long-term slope erosion and slope-failure hazards in seismically active regions, *Geomorphology*, *10*(14), 265–284, doi:10.1016/0169-555X(94)90021-3.
Keefer, D. K. (2002), Investigating landslides caused by earthquakes—A historical review, *Surv. Geophys.*, *23*(6), 473–510, doi:10.1023/A:1021274710840.
Keefer, D. K., and M. W. Manson (1998), Regional distribution and characteristics of landslides generated by the earthquake, *U.S. Geol. Surv. Prof. Pap. 1551-C*, U.S. Gov. Print. Off., Washington, D. C.
Kempton, J. J., and J. P. Stewart (2006), Prediction equations for significant duration of earthquake ground motions considering site and near source effects, *Earthquake Spectra*, *22*(4), 985–1013, doi:10.1193/1.2358175.
Khazai, B., and N. Sitar (2004), Evaluation of factors controlling earthquake-induced landslides caused by Chi-Chi earthquake and comparison with the Northridge and Loma Prieta events, *Eng. Geol.*, *71*(12), 79–95, doi:10.1016/S0013-7952(03)00127-3.
Kikuchi, M., and H. Kanamori (1991), Inversion of complex body waves—III, *Bull. Seismol. Soc. Am.*, *81*(6), 2335–2350.
Lacroix, P., B. Zavala, E. Berthier, and L. Audin (2013), Supervised method of landslide inventory using panchromatic SPOT5 images and application to the earthquake-triggered landslides of Pisco (Peru, 2007, M_w8.0), *Remote Sens.*, *5*(6), 2590–2616, doi:10.3390/rs5062590.
Larsen, I., D. Montgomery, and O. Korup (2010), Landslide erosion controlled by hillslope material, *Nat. Geosci.*, *3*(4), 247–251.
Lee, W. H. K., T. C. Shin, K. W. Kuo, K. C. Chen, and C. F. Wu (2001), CWB free-field strong-motion data from the 21 September Chi-Chi, Taiwan, earthquake, *Bull. Seismol. Soc. Am.*, *91*(5), 1370–1376, doi:10.1785/0120000744.
Legrand, D., S. Barrientos, K. Bataille, J. Cembrano, and A. Pavez (2011), The fluid-driven tectonic swarm of Aysen Fjord, Chile (2007) associated with two earthquakes ($M_w = 6.1$ and $M_w = 6.2$) within the Liquiñe-Ofqui fault zone, *Cont. Shelf Res.*, *31*(3), 154–161, doi:10.1016/j.csr.2010.05.008.
Leonard, M. (2010), Earthquake fault scaling: Self-consistent relating of rupture length, width, average displacement, and moment release, *Bull. Seismol. Soc. Am.*, *100*(5A), 1971–1988.
Li, G., A. J. West, A. L. Densmore, Z. Jin, R. N. Parker, and R. G. Hilton (2014), Seismic mountain building: Landslides associated with the 2008 Wenchuan earthquake in the context of a generalized model for earthquake volume balance, *Geochem. Geophys. Geosyst.*, *15*, 833–844, doi:10.1002/2013GC005067.
Li, X., Z. Zhou, H. Yu, R. Wen, D. Lu, M. Huang, Y. Zhou, and J. Cu (2008), Strong motion observations and recordings from the great Wenchuan earthquake, *Earthquake Eng. Eng. Vibr.*, *7*(3), 235–246, doi:10.1007/s11803-008-0892-x.
Liao, H.-W., and C. Lee (2000), Landslides triggered by Chi-Chi earthquake, in *Proceedings of the 21st Asian Conference on remote Sensing*, vol. 1, pp. 383–388, Asian Association on Remote Sensing, Taipei, Taiwan.
Lin, G.-W., H. Chen, N. Hovius, M.-J. Horng, S. Dadson, P. Meunier, and M. Lines (2008), Effects of earthquake and cyclone sequencing on landsliding and fluvial sediment transfer in a mountain catchment, *Earth Surf. Processes Landforms*, *33*(9), 1354–1373, doi:10.1002/esp.1716.
Mahdavifar, M. R., S. Solaymani, and M. K. Jafari (2006), Landslides triggered by the Avaj, Iran earthquake of June 22, 2002, *Eng. Geol.*, *86*(23), 166–182, doi:10.1016/j.enggeo.2006.02.016.
Malamud, B. D., D. L. Turcotte, F. Guzzetti, and P. Reichenbach (2004), Landslides, earthquakes, and erosion, *Earth Planet. Sci. Lett.*, *229*(12), 45–59, doi:10.1016/j.epsl.2004.10.018.
Marc, O., and N. Hovius (2015), Amalgamation in landslide maps: Effects and automatic detection, *Nat. Hazards Earth Syst. Sci.*, *15*(15), 723–733, doi:10.5194/nhess-15-723-2015.
Marc, O., N. Hovius, P. Meunier, T. Uchida, and S. Hayashi (2015), Transient changes of landslide rates after earthquakes, *Geology*, *43*, 883–886, doi:10.1130/G36961.1.
Mathur, L. (1953), Assam earthquake of 15th August 1950—A short note on factual observations, in *A Compilation of Papers on the Assam earthquake of August, 15, 1950*, vol. 1, edited by M. B. Ramachandra Rao, pp. 56–60, Cent. Board of Geophys. Publ., Natl. Geophys. Res. Inst., Hyderabad, India.
McColl, S. T., T. R. H. Davies, and M. J. McSaveney (2012), The effect of glaciation on the intensity of seismic ground motion, *Earth Surf. Processes Landforms*, *37*(12), 1290–1301, doi:10.1002/esp.3251.
McGinty, P., D. Darby, and J. Haines (2001), Earthquake triggering in the Hawke's Bay, New Zealand, region from 1931 to 1934 as inferred from elastic dislocation and static stress modeling, *J. Geophys. Res.*, *106*(B11), 26,593–26,604, doi:10.1029/2000JB000031.
Meunier, P., N. Hovius, and A. J. Haines (2007), Regional patterns of earthquake-triggered landslides and their relation to ground motion, *Geophys. Res. Lett.*, *34*, L20408, doi:10.1029/2007GL031337.
Meunier, P., N. Hovius, and J. A. Haines (2008), Topographic site effects and the location of earthquake induced landslides, *Earth Planet. Sci. Lett.*, *275*(34), 221–232, doi:10.1016/j.epsl.2008.07.020.
Meunier, P., T. Uchida, and N. Hovius (2013), Landslide patterns reveal the sources of large earthquakes, *Earth Planet. Sci. Lett.*, *363*, 27–33.
Molnar, P., and D. Qidong (1984), Faulting associated with large earthquakes and the average rate of deformation in central and eastern Asia, *J. Geophys. Res.*, *89*(B7), 6203–6227, doi:10.1029/JB089iB07p06203.
Molnar, P., R. S. Anderson, and S. P. Anderson (2007), Tectonics, fracturing of rock, and erosion, *J. Geophys. Res.*, *112*, F03014, doi:10.1029/2005JF000433.
Newmark, N. (1965), Effects of earthquakes on dams and embankments, *Geotechnique*, *15*(2), 139–159.
Oglesby, D. D., R. J. Archuleta, and S. B. Nielsen (2000), The three-dimensional dynamics of dipping faults, *Bull. Seismol. Soc. Am.*, *90*(3), 616–628, doi:10.1785/0119990113.
Owen, L. A., U. Kamp, G. A. Khattak, E. L. Harp, D. K. Keefer, and M. A. Bauer (2008), Landslides triggered by the 8 October 2005 Kashmir earthquake, *Geomorphology*, *94*(12), 1–9, doi:10.1016/j.geomorph.2007.04.007.
Parise, M., and R. W. Jibson (2000), A seismic landslide susceptibility rating of geologic units based on analysis of characteristics of landslides triggered by the 17 January, 1994 Northridge, California earthquake, *Eng. Geol.*, *58*(34), 251–270, doi:10.1016/S0013-7952(00)00038-7.
Parker, R., A. Densmore, N. Rosser, M. De Michele, Y. Li, R. Huang, S. Whadcoat, and D. Petley (2011), Mass wasting triggered by the 2008 Wenchuan earthquake is greater than orogenic growth, *Nat. Geosci.*, *4*(7), 449–452.
Pathier, E., E. Fielding, T. Wright, R. Walker, B. Parsons, and S. Hensley (2006), Displacement field and slip distribution of the 2005 Kashmir earthquake from SAR imagery, *Geophys. Res. Lett.*, *33*, L20310, doi:10.1029/2006GL027193.
Pearce, A. J., and C. L. O'Loughlin (1985), Landsliding during a M 7.7 earthquake: Influence of geology and topography, *Geology*, *13*(12), 855–858, doi:10.1130/0091-7613(1985)13<855:LDAMEI>2.0.CO;2.
Picozzi, M., S. Parolai, and S. M. Richwalski (2005), Joint inversion of H/V ratios and dispersion curves from seismic noise: Estimating the *S*-wave velocity of bedrock, *Geophys. Res. Lett.*, *32*, L11308, doi:10.1029/2005GL022878.
PWRI (2009), Report for basic data collection about seismic landslides [in Japanese], *Debris flow and Volcano Team Tech. Rep.*, p. 56, Public Work Res. Inst., Tsukuba, Japan.
Rodriguez, C. E., J. J. Bommer, and R. J. Chandler (1999), Earthquake-induced landslides: 1980–1997, *Soil Dyn. Earthquake Eng.*, *18*(5), 325–346, doi:10.1016/S0267-7261(99)00012-3.

Ruiz, S., E. Kausel, J. Campos, G. R. Saragoni, and R. Madariaga (2011), Identification of high frequency pulses from earthquake asperities along Chilean subduction zone using strong motion, *Pure Appl. Geophys.*, *168*(1–2), 125–139, doi:10.1007/s00024-010-0117-x.
Schmidt, K. M., and D. R. Montgomery (1995), Limits to relief, *Science*, *270*(5236), 617–620, doi:10.1126/science.270.5236.617.
Schmidt, K. M., and D. R. Montgomery (1996), Rock mass strength assessment for bedrock landsliding, *Environ. Eng. Geosci.*, *2*(3), 325–338, doi:10.2113/gseegeosci.II.3.325.
Schuster, R. L., A. S. NietoThomas, T. D O'Rourke, E. Crespo, and G. Plaza-Nieto (1996), Mass wasting triggered by the 5 March 1987 Ecuador earthquakes, *Eng. Geol.*, *42*(1), 1–23.
Sleep, N. H. (2011a), Seismically damaged regolith as self-organized fragile geological feature, *Geochem. Geophys. Geosyst.*, *12*, Q12013, doi:10.1029/2011GC003837.
Sleep, N. H. (2011b), Deep-seated downslope slip during strong seismic shaking, *Geochem. Geophys. Geosyst.*, *12*, Q12001, doi:10.1029/2011GC003838.
Stark, C. P., and F. Guzzetti (2009), Landslide rupture and the probability distribution of mobilized debris volumes, *J. Geophys. Res.*, *114*, F00A02, doi:10.1029/2008JF001008.
Stark, C. P., and N. Hovius (2001), The characterization of landslide size distributions, *Geophys. Res. Lett.*, *28*(6), 1091–1094, doi:10.1029/2000GL008527.
Stein, R. S., and G. Ekström (1992), Seismicity and geometry of a 110-km-long blind thrust fault 2. Synthesis of the 1982–1985 California earthquake sequence, *J. Geophys. Res.*, *97*(B4), 4865–4883.
Stevens, C., R. McCaffrey, E. Silver, Z. Sombo, P. English, and J. Van der Kevie (1998), Mid-crustal detachment and ramp faulting in the Markham Valley, Papua New Guinea, *Geology*, *26*(9), 847–850.
Suarez, G., M. Pardo, J. Dominguez, L. Ponce, W. Montero, I. Boschini, and W. Rojas (1995), The Limon, Costa Rica earthquake of April 22, 1991: Back arc thrusting and collisional tectonics in a subduction environment, *Tectonics*, *14*(2), 518–530, doi:10.1029/94TC02546.
Sun, J., Z.-K. Shen, R. Burgmann, M. Wang, L. Chen, and X. Xu (2013), A three-step maximum a posteriori probability method for InSAR data inversion of coseismic rupture with application to the 14 April 2010 M_w 6.9 Yushu, China, earthquake, *J. Geophys. Res. Solid Earth*, *118*, 4599–4627, doi:10.1002/jgrb.50244.
Tan, O., and T. Taymaz (2006), Active tectonics of the Caucasus: Earthquake source mechanisms and rupture histories obtained from inversion of teleseismic body waveforms, in *Postcollisional Tectonics and Magmatism in the Mediterranean Region and Asia*, edited by Y. Dilek and S. Pavlides, *Geol. Soc. Am. Spec. Pap.*, *409*, 531–578, doi:10.1130/2006.2409(25).
Tang, C., G. Ma, M. Chang, W. Li, D. Zhang, T. Jia, and Z. Zhou (2015), Landslides triggered by the 20 April 2013 Lushan earthquake, Sichuan Province, China, *Eng. Geol.*, *187*, 45–55, doi:10.1016/j.enggeo.2014.12.004.
Tatard, L., and J. R. Grasso (2013), Controls of earthquake faulting style on near field landslide triggering: The role of coseismic slip, *J. Geophys. Res. Solid Earth*, *118*, 2953–2964, doi:10.1002/jgrb.50215.
Terzaghi, K. (1950), Mechanism of landslides, in *Application of Geology to Engineering Practice (Berkey Volume)*, edited by S. Paige, pp. 83–123, Geol. Soc. Am., New York.
Voight, B., and J. Sousa (1994), Lessons from Ontake-san: A comparative analysis of debris avalanche dynamics, *Eng. Geol.*, *38*(3), 261–297, doi:10.1016/0013-7952(94)90042-6.
Wald, D., D. Helmberger, and T. Heaton (1991), Rupture model of the 1989 Loma Prieta earthquake from the inversion of strong-motion and broadband teleseismic data, *Bull. Seismol. Soc. Am.*, *81*(5), 1540–1572.
Wald, D., T. Heaton, and K. Hudnut (1996), The slip history of the 1994 Northridge, California, earthquake determined from strong-motion, teleseismic, GPS, and leveling data, *Bull. Seismol. Soc. Am.*, *86*(1B), S49–S70.
Wallace, T. C., and T. Lay (1995), Chapter 3—Body waves and ray theory, in *Modern Global Seismology, Int. Geophys.*, vol. 58, pp. 70–115, Academic Press, New York, doi:10.1016/S0074-6142(05)80004-X.
Wang, D., and J. Mori (2012), The 2010 Qinghai, China, earthquake: A moderate earthquake with supershear rupture, *Bull. Seismol. Soc. Am.*, *102*(1), 301–308, doi:10.1785/0120110034.
Wartman, J., L. Dunham, B. Tiwari, and D. Pradel (2013), Landslides in Eastern Honshu induced by the 2011 Tohoku Earthquake, *Bull. Seismol. Soc. Am.*, *103*(2B), 1503–1521, doi:10.1785/0120120128.
Wei, S., et al. (2011), Superficial simplicity of the 2010 El Mayor-Cucapah earthquake of Baja California in Mexico, *Nat. Geosci.*, *4*(9), 615–618, doi:10.1038/ngeo1213.
Wen, K.-L. (1994), Non-linear soil response in ground motions, *Earthquake Eng. Struct. Dyn.*, *23*(6), 599–608, doi:10.1002/eqe.4290230603.
Wolinsky, M. A., and L. F. Pratson (2005), Constraints on landscape evolution from slope histograms, *Geology*, *33*(6), 477–480, doi:10.1130/G21296.1.
Xu, C., X. Xu, H. R. Pourghasemi, B. Pradhan, and J. Iqbal (2014a), Volume, gravitational potential energy reduction, and regional centroid position change in the wake of landslides triggered by the 14 April 2010 Yushu earthquake of China, *Arabian J. Geosci.*, *7*(6), 2129–2138, doi:10.1007/s12517-013-1020-4.
Xu, C., X. Xu, J. B. H. Shyu, W. Zheng, and W. Min (2014b), Landslides triggered by the 22 July 2013 Minxian-Zhangxian, China, M_w 5.9 earthquake: Inventory compiling and spatial distribution analysis, *J. Asian Earth Sci.*, *92*, 125–142, doi:10.1016/j.jseaes.2014.06.014.
Yagi, H., T. Yamasaki, and M. Atsumi (2007), GIS analysis on geomorphological features and soil mechanical implication of landslides caused by 2004 Niigata Chuetsu earthquake, *J. Jpn. Landslide Soc.*, *43*(5), 294–306.
Yagi, H., G. Sato, D. Higaki, M. Yamamoto, and T. Yamasaki (2009), Distribution and characteristics of landslides induced by the Iwate-Miyagi Nairiku earthquake in 2008 in Tohoku district, Northeast Japan, *Landslides*, *6*(4), 335–344.
Yoshida, S., and K. Koketsu (1990), Simultaneous inversion of waveform and geodetic data for the rupture process of the 1984 Naganoken-Seibu, Japan, earthquake, *Geophys. J. Int.*, *103*(2), 355–362.
Yuan, R.-M., Q.-H. Deng, D. Cunningham, C. Xu, X.-W. Xu, and C.-P. Chang (2013), Density distribution of landslides triggered by the 2008 Wenchuan earthquake and their relationships to peak ground acceleration, *Bull. Seismol. Soc. Am.*, *103*(4), 2344–2355, doi:10.1785/0120110233.
Zeng, Y., and C.-H. Chen (2001), Fault rupture process of the 20 September 1999 Chi-Chi, Taiwan, earthquake, *Bull. Seismol. Soc. Am.*, *91*(5), 1088–1098, doi:10.1785/0120000743.
Zhang, Y., R. Wang, Y.-T. Chen, L. Xu, F. Du, M. Jin, H. Tu, and T. Dahm (2014), Kinematic rupture model and hypocenter relocation of the 2013 Mw 6.6 Lushan earthquake constrained by strong-motion and teleseismic data, *Seismol. Res. Lett.*, *85*(1), 15–22, doi:10.1785/0220130126.